SENSOR COMPARISON FOR LOW-COST DYNAMIC FORCE MEASUREMENT IN MILLING

A Thesis Presented for the
Master of Science
Degree
The University of Tennessee, Knoxville

Zachary Douglas Mason
May 2022

ACKNOWLEDGEMENTS

I would like to thank my advisor, Dr. Schmitz, for his guidance and his help in completing this research. You gave me motivation when I needed it most and were always there to help. I would also like to thank my friends and colleagues Ross Zameroski, Gregory Corson, Jose Nazario, Dr. Tim No, Dr. Michael Gomez, and everyone at the Machine Tool Research Center (MTRC) for their help and support. I would also like to thank my family for their steadfast love, for which I will always be truly grateful.

ABSTRACT

Machine cutting forces are commonly measured using piezoelectric dynamometers. Such dynamometers can be prohibitively expensive and may still require extensive post processing. Previous work used a low-cost single degree of freedom constrained motion dynamometer (CMD) in conjunction with a knife edge sensor to determine the cutting forces through inverse force filtering. In that approach, the measured displacement of the CMD was transformed into the frequency domain by the fast Fourier transform (FFT) and convolved with the inverted receptance frequency response function (FRF) to yield force in the frequency domain. The force was then converted to the time domain using the inverse FFT. This research seeks to expand upon that inverse force filtering approach by measuring displacement, velocity, and acceleration and calculating force using the inverted FRF corresponding to each measurement type. Displacement was again measured by a knife edge sensor. The velocity was measured using a laser vibrometer, and the acceleration was measured using both a solid state accelerometer, and a piezoelectric accelerometer. The frequency domain velocity was convolved with the inverted mobility FRF to obtain the frequency domain force, and the acceleration signals were convolved with the inverted accelerance FRF. The forces determined from the velocity required a low-pass and high-pass filter to attenuate unwanted signal gain associated with the inverted mobility FRF. The acceleration signals required both a high-pass filter to attenuate the unwanted signal gain at low frequencies due to the inverted accelerance and a low-pass filter to attenuate affects due to high frequency noise associated with the accelerometers. The displacement-based forces showed good agreement with the forces determined by a time domain simulation and those measured by a commercially-available piezoelectric dynamometer. However, the forces determined from the velocity and acceleration signals suffered from loss of the average (or mean, or zero-frequency/DC) component of the signal, which meant that only the peak-to-valley force values could be compared to the other results.

TABLE OF CONTENTS

LIST OF TABLES

LIST OF FIGURES

CHAPTER 1: INTRODUCTION

Introduction

This thesis describes the measurement of dynamic cutting forces in a computer numerically controlled (CNC) milling machine. Cutting force measurements in CNC milling are typically performed by costly three-axis dynamometers, such as the Kistler type 9257B piezoelectric three-component dynamometer used in this study. However, such devices may be prohibitively expensive (approximately $100,000) and may still require extensive post-processing of the measured force data. To provide an alternative, previous work has measured cutting forces using a single degree of freedom (SDOF) constrained motion dynamometer (CMD) in conjunction with an optical interrupter and knife edge (i.e., knife edge sensor) to measure the displacement of a workpiece attached to the CMD's moving stage [1-4]. During milling, the optical interrupter outputs a voltage corresponding to the knife edge displacement, which represents the workpiece motion (because it is attached to the CMD's movable stage) [5]. After the cutting tests, the time dependent displacement data measured by the knife edge sensor is converted to the frequency domain using the fast Fourier transform (FFT) and convolved with the CMD's inverted frequency response function (FRF) to yield the frequency domain force. The frequency domain force is converted back to the time domain by the inverse FFT to give the time domain cutting force.

This research extends the previous work by using two different accelerometers and a laser vibrometer to measure the CMD system's acceleration and velocity and computing the force from these new signals, again using the CMD's structural dynamics. The resulting forces are compared to those measured by a commercially available piezoelectric dynamometer, the CMD with a knife edge sensor, and the forces predicted by a time domain simulation of the milling process to determine the efficacy of these acceleration and velocity sensors.

Literature Review

Cutting force is a primary consideration in machining, where a sharp cutting edge is used to shear away material to leave the desired part geometry [6-8]. Cutting forces are highly sensitive to changes in cutting conditions, which are prescribed by the machining process [9-10, 12]. As a result, cutting forces may be used to determine optimized machining parameters. For example, adaptive feed rate control may be applied to maintain the cutting force within predetermined bounds [6-9]. Cutting force can also be used to evaluate tool wear and to determine whether chatter occurred during a machining operation [6-7, 9-18].

The cutting force is a vector quantity, which means that both a magnitude and direction are required to characterize it [13-15]. To quantify cutting forces, their effects on the machining system may be measured using displacement, velocity, or acceleration sensors, and then relating these signals to force through a known physical relationship [13-15].

The most common method to measure cutting forces is the use of multi-degree-of-freedom piezoelectric dynamometers (PDs), which are typically comprised of a number of piezoelectric transducers [13-14]. The transducers produce a charge and a corresponding voltage proportional to the deformation of the piezoelectric material within them due to an external force [13]. When a force is applied to the PD during machining, a proportional deflection of the piezoelectric material occurs, producing a voltage which is also proportional to the force [6-7, 13-15]. Given that a PD is a dynamic system, care must be taken when operating near one of the PD's natural frequencies in order to avoid the amplification of input force signals by the system dynamics [3].

Prior work has examined various designs for force measurement dynamometers. A dynamometer based on two coupled, single degree off freedom flexures was presented by Schmitz et al. [19]. In this setup, the interaction of the flexures produced vibration modes that bookended the bandwidth of interest. Korkut [20] used strain gauges mounted to four octagonal rings between two plates to determine cutting forces. Yadiz et al. [21-22] similarly used octagonal rings and strain-gauge based sensors to measure the static and dynamic cutting forces as well as torque. Transchel et al. [23] used pre-loaded piezoelectric sensors to increase the dynamic stiffness and created a dynamometer capable of measuring up to 5 kHz. Totis et al. [24-25] used three high-sensitivity tri-axial piezoelectric force sensors to create a plate-type dynamometer with increased bandwidth due to the high natural frequency resulting from the novel sensor configuration.

Researchers have also explored the integration of force sensors into the machine spindle and machine tool [26-30]. A spindle-based torque dynamometer using strain gauge-based sensors placed between the holder and the tool was developed by Smith et al. [33]. Altintas and Park [31-32] developed a Spindle Integrated Force Sensor using piezoelectric sensors embedded in a circular arrangement within the spindle housing and a Kalman filter. Aoyama and Ishii [33] detected the intensity and direction of the magnetic field related to the material strain to determine cutting forces using the Villari effect. Ettrichratz et al. [34] used a carbide sensor plate with piezoceramic layers mounted next to a cutting insert to accurately measure force due to the proximity of the sensor to the cutting edge.

Prior efforts have also attempted to obtain accurate cutting forces using post-processing techniques that compensate for dynamometer dynamics. Tlusty et al. [11] and Tounsi et al. [35-36] improved the force measuring accuracy by estimating inertial and damping errors. Altintas and Park [31-32, 37-38] removed the structural dynamic influence of the spindle transfer functions within the Spindle Integrated Force Sensor system using a disturbance Kalman filter. Totis et al. [39] also improved force measurement frequency bandwidth using Kalman filtering. Castro et al. [40] used the system's transmissibility matrix to attenuate high frequency amplification due to "cross-talk" between component axes of the dynamometer. Korkmaz and Ozdoganlar et al. [41-44] used a 3x3 force-to-force frequency response function (FRF) inverse filter to compensate dynamometer distortions at high frequencies. Scippa et al. [45] compensated for high frequency attenuation of cutting forces using "band-fitting" and "parallel elaboration" filters. These approaches all rely on either inverse compensation filters or Kalman filters, which themselves rely on the system frequency response functions (FRFs) [21-22, 37-49]. Although consistent results can be produced using these approaches, their accuracy depends on the proper fitting of the multi-mode FRF [46-49].

As previously mentioned, prior work by Gomez and Schmitz [3] used a single degree of freedom CMD and displacement sensor to measure forces through inverse force filtering. In this approach, the displacement of the CMD was measured and converted to the frequency domain using the fast Fourier transform (FFT) and convolved with the inverse system FRF to give the frequency domain force. The frequency domain force was further convolved with a low-pass filter to attenuate high frequency amplification of the displacement signal due to the inverted FRF. The frequency domain force was then converted to the time domain using the inverse FFT.

CHAPTER 2: BACKGROUND

Milling Description

In milling, material is removed from a workpiece by a rotating tool with defined edges [6]. The tool and its associated holder are typically attached to a spindle that supplies the rotational speed, torque, and power of the tool. In three-axis milling, the tool-holder-spindle combination moves relative to the workpiece using three perpendicular axes. Commonly, the axes are labeled x, y, and z, with the latter being the tool axis.

Many types of tools may be used in milling to perform a number of applications, such as contour, end, face, and peripheral milling. In end milling, the tool removes material along its radial, z, axis as it advances radially relative to the workpiece. End mills may have teeth ground directly into the tool or may use replaceable inserts clamped to tool periphery. Often, the edge of the end mill is inclined to the vertical axis (i.e., the helix angle) to decrease the edge pressure during cutting and to spread the material being removed over a larger surface.

The individual pieces of material removed by the tool are referred to as chips. In end milling, the chip width, b, is determined by the axial depth of cut and the helix angle of the tool. The chip thickness, $h(t)$, is a time dependent measurement of the size of the chip in the tool's radial direction. It is a product of the feed per tooth and the sine of the angle of the tooth as it rotates to remove material from the workpiece. The feed per tooth, f_t is the ratio of the linear feed rate f of the tool relative to the product of the spindle speed, Ω and the number of teeth, N_t. It is given by Equation 1.

$$f_t = \frac{f}{\Omega N_t} \tag{1}$$

In reality, as the tool advances during end milling operations, it tends to follow a cycloidal path. However, given the relatively small magnitude of linear advancement in comparison to the rotational velocity of the cutting edge, an approximation can be made that each cutting surface of the tool creates a series of successive circles, with each circle offset from the previous circle by the feed per tooth. In addition to the feed per tooth, the time dependent chip thickness also depends on the cutting operation employed. Two common types of end milling are up milling and down milling. In up milling, the chip thickness increases as the tooth travels through the workpiece, whereas in down milling, the chip thickness decreases as the cutting edge travels through the workpiece.

A cutting force model is used to relate the chip width and thickness to the required force to shear away the chip. The force is typically assumed to be proportional to the product of the specific cutting force coefficients and the area of the chip produced. As the area increases, the cutting force increases. However, this model may lead to discrepancies when compared to measured cutting forces, as cutting force coefficients are process dependent and reliant on the tool workpiece combination, rather than just the material. Two factors that highlight this fact are the edge effects and the cutting speed dependence. As the radius of a cutting edge is not exactly zero, rubbing occurs between the cutting edge and workpiece as chip thickness is reduced. The rubbing effect leads to forces greater than would be expected from just the specific force times the chip area. Rubbing can be incorporated to the force model by adding a force component that is proportional to the axial depth of cut only. In doing so, a nonzero force is maintained even when the chip thickness approaches zero. This DC offset is known as the “edge effect”. A force model can then be defined that relies on both cutting and rubbing coefficients. The force model is seen in Equation 2, Equation 3, and Equation 4 below.

$$F_x = k_t b f_t \sin(\phi)\cos(\phi) + k_{te} b \cos(\phi) + k_n b f_t \sin^2(\phi) + k_{ne} b \sin(\phi) \tag{2}$$

$$F_y = k_t b f_t \sin^2(\phi) + k_{te} b \sin(\phi) - k_n b f_t \sin(\phi)\cos(\phi) - k_{ne} b \sin(\phi) \tag{3}$$

$$F_z = -k_a b f_t \sin(\phi) - k_{ae} b \tag{4}$$

In the force model, k_t and k_n are the specific force coefficient components tangential and normal to the tool, respectively, and are associated with cutting. The edge effects are represented by the k_{te} and k_{ne} terms, which correspond to the rubbing effects in the tangential and normal directions respectively. Similarly, the terms k_a and k_{ae} represent the cutting force coefficient and the rubbing coefficient in the axial direction of the tool. F_x, F_y, and F_z represent the force in in the x, y, and z directions, respectively. The ϕ term represents the tool rotation angle.

To determine k_t, k_{te}, k_n, k_{ne}, k_a, and k_{ae}, a linear regression is performed using the average cutting forces measured over a range of feeds per tooth values by a dynamometer [6]. The linear regression for the x-direction takes the form seen in Equation 5.

$$\bar{F}_{x,i} = a_{0x} + a_{1_x} f_{t,i} + E_i \tag{5}$$

In this form, a_0 represents the intercept and the a_1 term represents the slope of the line. The E_i term is the error between the line formed by $a_0 + a_1 f_{t,i}$ and the average force values for each feed per tooth. The $\bar{F}$ term represents the average force. The intercept term is determined according to Equation 6, and the slope term is determined from Equation 7.

$$a_0 = \frac{1}{n}\sum_{i=1}^{n} \bar{F}_i - a_{1x}\frac{1}{n}\sum_{i=1}^{n} f_{t,i} \tag{6}$$

$$a_1 = \frac{n\sum_{i=1}^{n} f_{t,i}\bar{F}_{x,i} - \sum_{i=1}^{n} f_{t,i}\bar{F}_{x,i}}{\sum_{i=1}^{n} f_{t,i}^2 - \left(\sum_{i=1}^{n} f_{t,i}\right)^2} \tag{7}$$

For more than two points, the slope and intercept are found by minimizing the error terms according to Equation 8.

$$\sum_{i=1}^{n} E_i^2 = \sum_{i=1}^{n}\left(\bar{F}_i - a_0 - a_1 f_{t,i}\right)^2 \tag{8}$$

After determining the slope and intercept values for the x , y, and z directions, the cutting force and edge coefficients are determined by solving Equation 9, Equation 10, and Equation 11.

$$\bar{F}_x = \left[\frac{N_t b f_t}{8\pi}\left(-k_t \cos(2\phi) + k_n(2\phi - \sin(2\phi))\right) + \frac{N_t b}{2\pi}(k_{te}\sin(\phi) - k_{ne}\cos(\phi))\right]_{\phi_s}^{\phi_e} \quad (9)$$

$$\bar{F}_y = \left[\frac{N_t b f_t}{8\pi}(k_t(2\phi - \sin(2\phi)) + k_n\cos(2\phi)) - \frac{N_t b}{2\pi}(k_{te}\cos(\phi) + k_{ne}\sin(\phi))\right]_{\phi_s}^{\phi_e} \quad (10)$$

$$\bar{F}_z = \left[\frac{N_t b}{2\pi}(k_a f_t \cos(\phi) - k_{ae}\phi)\right]_{\phi_s}^{\phi_e} \quad (11)$$

The ϕ_s and ϕ_e terms are the start and exit angles. For up milling, the start angle is 0 degrees, and the exit angle is found using Equation 12.

$$\phi_e = \cos^{-1}\left(\frac{r-a}{r}\right) \quad (12)$$

The a term is the radial depth of cut. The r term is the radius of the tool. For down milling, the exit angle is 180 degrees. The start angle for down milling is given by Equation 13.

$$\phi_s = 180 - \cos^{-1}\left(\frac{r-a}{r}\right) \quad (13)$$

Time Domain Simulation

In this study, a time domain simulation is used that is based on the "Regenerative Force, Dynamic Deflection" model described by Smith and Tlusty [50]. The time domain simulation provides local force and vibration data for a given set of cutting conditions by using numerical integration to solve time-delayed differential equations of motions [6]. The simulation is capable of incorporating complicated tool geometries, as well as nonlinearities that occur if a tooth leaves the cut due to large vibrations.

The time domain simulation uses incrementing tooth angle values as a basis for its calculation. To do this, it creates an array of possible tooth angles based on the number of steps per revolution. Each entry in the array is offset by an amount $d\phi$ determined according to Equation 14.

$$d\phi = \frac{360}{SR}\ (deg) \quad (14)$$

The SR term is the number of steps per revolution of the cutter, which is determined by the stipulated spindle speed and highest natural frequency of the system. A time step dt is created according to Equation 15.

$$dt = \frac{60}{\Omega \cdot \mathrm{SR}} \text{ (sec)} \tag{15}$$

For each step in the simulation, the instantaneous chip thickness is determined using the vibration of the current and previous tooth at a given angle according to Equation 16:

$$h(t) = f_t \sin(\phi) + n(t - \tau) - n(t) \tag{16}$$

The f_t term is the feed per tooth, ϕ is the current tooth angle, τ is the tooth passing period, and t is the current time. In this expression, $f_t \sin(\phi)$ is the nominal chip thickness, the $n(t - \tau)$ term represents the vibration contributions of the tool and workpiece along the surface normal due to the previous tooth, and the $n(t)$ term represents the vibration contribution projected on to the normal surface due to the current tooth. The projection of the vibration onto the normal surface is obtained according to Equation 17:

$$n = x \sin(\phi) - y \cos(\phi) \tag{17}$$

The cutting forces are calculated at each step according to Equation 18 and Equation 19:

$$F_x = (k_n bh(t) + k_{ne} b) \sin(\phi) - (k_t bh(t) + k_{te} b) \cos(\phi) \tag{18}$$

$$F_y = (k_n bh(t) + k_{ne} b) \cos(\phi) + (k_t bh(t) + K_{te} b) \sin(\phi) \tag{19}$$

The cutting force coefficients in these equations are the experimentally determined coefficients previously discussed. It is important to note that if $h(t)$ is less than or equal to zero, F_x and F_y are set to zero, which incorporates the nonlinearity that occurs when the tool leaves the workpiece due to large vibrations.

Once the forces have been found, they are used to find the solutions to the differential equations of motion for both the tool and workpiece. Equation 20 and Equation 21 present the general equations of motion in the *x* and *y* directions respectively.

$$m_x \ddot{x} + c_x \dot{x} + k_x x = F_x \tag{20}$$

$$m_y \ddot{y} + c_y \dot{y} + k_y y = F_y \tag{21}$$

The m, c, and k are the modal mass, damping, and stiffness terms. The $\ddot{x}$ and $\ddot{y}$ terms represent the acceleration in the x direction and y direction respectively. Similarly, the $\dot{x}$ and $\dot{y}$ terms represent the velocity, and the x and y terms represent the displacement in the x and y directions.

The acceleration terms for the current step are found by rearranging Equation 20 and Equation 21 into Equation 22 and Equation 23.

$$\ddot{x}(i) = \frac{F_x(i) - c_x \dot{x}(i-1) - k_x x(i-1)}{m_x} \tag{22}$$

$$\ddot{y}(i) = \frac{F_y(i) - c_y\dot{y}(i-1) - k_y y(i-1)}{m_y} \tag{23}$$

The $(i-1)$ terms represent quantities found in the previous time step of the simulation, although the initial $(i-1)$ terms are zero (for zero initial conditions). The (i) terms represent quantities determined during the current time step of the simulation. After obtaining the acceleration, modified Euler integration is used to find the velocity terms of the current step according to Equation 24 and Equation 25.

$$\dot{x}(i) = \dot{x}(i-1) + \ddot{x}(i)\,dt \tag{24}$$

$$\dot{y}(i) = \dot{y}(i-1) + \ddot{y}(i)\,dt \tag{25}$$

With the velocities found, the displacements are calculated using Equation 26 and Equation 27.

$$x(i) = x(i-1) + \dot{x}(i) \tag{26}$$

$$y(i) = y(i-1) + \dot{y}(i) \tag{27}$$

Once the current acceleration, position, and velocity have been found, the tooth angle and time are advanced, and the simulation repeats.

CMD

A constrained motion dynamometer (CMD) was used to measure the forces in this research. The CMD used was a monolithic design made from 6061-T6 aluminum and was the same design used by Gomez [51]. The design includes a moving platform connected to a frame by four leaf-type flexure elements in a four-bar linkage arrangement. The flexures behave as simple parallel rectilinear springs, which behave linearly over a certain displacement range. This design includes a kinematic over constraint, but this allows for elastic averaging of errors in bar lengths without introducing assembly errors. As the platform moves, the flexure leaves undergo elastic deformation, creating strains in the leaves that are resisted by the frame. The flexures act as a guide for the platform, constraining its motion to be perpendicular to the leaves.

The CMD flexure leaves dimensions are given in Table 2.1 CMD flexure leaf dimensions. The aluminum chosen for the CMD has a modulus, E, of 69 GPa and a yield strength, σ_y of 276 MPa. To allow the leaf deflection to remain elastic, the maximum allowable stress, $\sigma_{allowable}$, of the flexure element was selected to be 60% of the yield strength (160 MPa). The maximum allowable displacement of the leaf, $x_{allowable}$, was calculate using Equation 28.

Table 2.1 CMD flexure leaf dimensions.

Length, L (mm)	Width, b (mm)	Thickness, t (mm)	Radius, R (mm)
10	44.5	1.27	3.2

$$x_{allowable} = \frac{\sigma_{allowable} L^2}{3Et} \cong \pm 50\ \mu m \tag{28}$$

Nonlinearities from the doubly clamped elements are avoided by limiting the deflections to half the flexure thickness, and here the maximum allow deflection is significantly less than the half of the leaf thickness (0.6 mm).

The force range is found using Hooke's law. The spring constant of the structure is calculated using Equation 29.

$$K_{eq} = nK = \frac{n12EI}{L^3} \tag{29}$$

The n term is the number of flexure elements, which is four in this case. The I term is the second moment of area and can be found using Equation 30.

$$I = \frac{bt^3}{12} \tag{30}$$

Using the dimensions of the dynamometer, the spring constant is found to be, $K_{eq} = 1.5 \times 10^7 \frac{N}{m}$. With this the CMD force range can be found to be approximately $\pm$ 1500 N.

Optical Interrupter

The displacement of the CMD was measured using an optical interrupter in conjunction with a knife edge blade (together knife edge sensor, or KES). The KES has previously been used to measure the CMD displacement by Gomez [51]. The optical interrupter (ROHM RPI-0352E) comprises an optical transmitter and an optical receiver. A light beam emitted from the transmitter is picked up by the optical receiver, which outputs a corresponding voltage. The knife edge blocks a portion of the beam, reducing the amount of light measured by the detector, and changing the voltage output. As the CMD stage moves, the relative motion between the optical interrupter and the knife edge changes the amount of light detected and the voltage output by the sensor.

The optical sensor was attached to the bottom of the CMD's frame, while the knife edge was attached to the moving stage. At zero displacement, the knife edge was positioned such that it partially interrupted the beam. The optical interrupter nominally measures about 4 V when unimpeded. The length of the knife edge was adjusted so that the end of the blade was halfway through the light beam at zero displacement, which was determined by a measurement of half the nominal voltage.

The KES has previously been used to measure the displacement of the displacement of the CMD used in this experiment. From that experiment a, displacement sensitivity coefficient of 0.083 mm/V was determined. To check the accuracy of the KES, the displacement of a workpiece measured by the KES was compared to the displacement measured using a laser vibrometer to ensure agreement.

Laser Vibrometer

A laser vibrometer was used to measure the velocity of the CMD/workpiece system. The laser vibrometer (LV) consisted of a Polytec VibroFlex Compact VFX-I-130 with VibroFlex Connext VFX-F-110 Front End laser vibrometer.

The LDV provides non-contact velocity measurements using the Doppler effect. The LV emits a laser with frequency f. A target, in this case a workpiece, with its own velocity perceives a frequency f' due to the motion of the target relative to the light beam. The moving target transmits f' back to the laser vibrometer which sees a frequency of f''. The frequency of the emitted light f is then compared to the frequency of the received light f'', and the velocity, v, is found using Equation 31, where λ is the light wavelength.

$$v = \frac{(f'' - f)\lambda}{2} \tag{31}$$

The LV calibration coefficient was determined by selecting the lowest bandwidth option that covered the expected frequency range, in this case 20 kHz. Then a range option was selected that most closely matched the maximum expected velocity of the workpiece. For this experiment, a range of 500 mm/s was chosen. From this, a sensitivity coefficient of 250 mm/s/V was automatically calculated by the LV.

Solid State Accelerometer

The solid state accelerometer (SSA) was a microelectromechanical systems (MEMS) capacitance type accelerometer. The SSA (ADXL 1003z) is comprised of a polysilicon surface micromachined structure suspended over a silicon wafer by polysilicon springs [52]. Independent differential capacitors and differential capacitors attached to the polysilicon surface measure the deflection of the surface caused by an acceleration. The acceleration causes imbalance within the capacitors, resulting in an output proportional to the acceleration.

The SSA calibration coefficient was selected using the documentation provided with the sensor. From a chart of the sensitivity versus supply voltage, a calibration coefficient of 10 mV/g was determined based on an input voltage of 5 V.

Piezoelectric Accelerometer

The acceleration was also measured by a piezoelectric accelerometer (PA). The PA (PCB Piezotronics 352C23 ICP accelerometer) is comprised of a quartz crystal with a proof mass [53]. An acceleration leads to a deflection in the proof mass and a corresponding stress in the crystal. The stress induces a charge in the crystal due to the piezoelectric effect, which is then amplified and converted to a voltage.

The PA had previously been calibrated by the manufacturer, so the calibration constant used was supplied by the manufacturer.

Piezoelectric Dynamometer

The piezoelectric dynamometer (PD) is a quartz three component dynamometer capable of measuring force in three directions (Kistler 9257B). Four three-component force sensors are fitted under a high preload between two plates. Each force sensor has three pairs of quartz plates, with one pair sensitive to pressure in the z direction, and the others sensitive to shear in the x and y directions.

CHAPTER 3: EXPERIMENTAL SETUP AND PROCEDURE

Constrained Motion Dynamometer (CMD) Setup

The experimental setup began with the placement of the CMD on the machine table (Haas VF-4 computer numerically controlled machining center). The CMD was oriented such that its moving stage's flexible direction was aligned with the machine x direction. Alignment of the CMD with the machine x-direction was done using a dial indicator attached to the machine spindle.

Next, a housing for the two accelerometers (solid state and piezoelectric) was bolted to the CMD. The housing was 3D printed from ABS plastic using a 100% infill. The solid state accelerometer (SSA, Analog Devices ADXL 1003z) and piezoelectric accelerometer (PA, PCB Piezotronics 352C23) were attached to the housing and the housing was bolted to the CMD. The housing was also aligned with the machine x direction using the dial indicator to ensure the accelerometers were oriented in the x-direction.

The SSA was attached to the housing using four M3 bolts inserted through cutouts within the SSA and into inserts that were heat set into the plastic housing. The SSA was placed on the housing so that its sensitive axis was along the machine x-direction. The PA was attached to the side of the housing using modal wax, such that its sensitive axis was also aligned with the machine x-direction.

The knife edge sensor (KES) was attached to the bottom of the CMD, with the optical interrupter (ROHM RPI-0352E) attached to the stationary support structure of the CMD, and the knife edge (blade) attached to moving stage. A 51 mm by 64 mm 1018 cold rolled steel workpiece was attached to the CMD moving stage using bolts inserted through pre-drilled holes in the workpiece. The laser vibrometer (LV, Polytec VibroFlex Compact VFX-I-130 and a VibroFlex Connext VFX-F-110 Front End) was placed outside of the machine, such that the laser was aligned with the machine x-direction and reflected off the positive x-direction face of the workpiece. A cardboard tube was setup within the machine to prevent chips from entering the path of the laser beam. Additionally, reflective tape was used to calibrate the laser, but was later removed. The CMD setup can be seen in Figure 3.1. Setup of the CMD, showing the workpiece, housing, SSA, PA, LV (reflection point), and the KES. The outputs from the KES, LV, SSA, and PA were measured by a Data Translation DT9837B dynamic signal analyzer using the SpinScope data acquisition software from Manufacturing Laboratories, Inc. All signals were simultaneously recorded during milling trials using a sampling rate of 25 kHz.

Piezoelectric Dynamometer (PD) Setup

The PD (Kistler 9257B) was placed on the machine table such that its positive x direction was aligned with the machine's negative y direction, and its positive y axis was aligned with the machine's negative x direction. This was done in order to allow the wiring of the PD pass through the machine's side window. The PD and the workpiece can be seen in Figure 3.2.

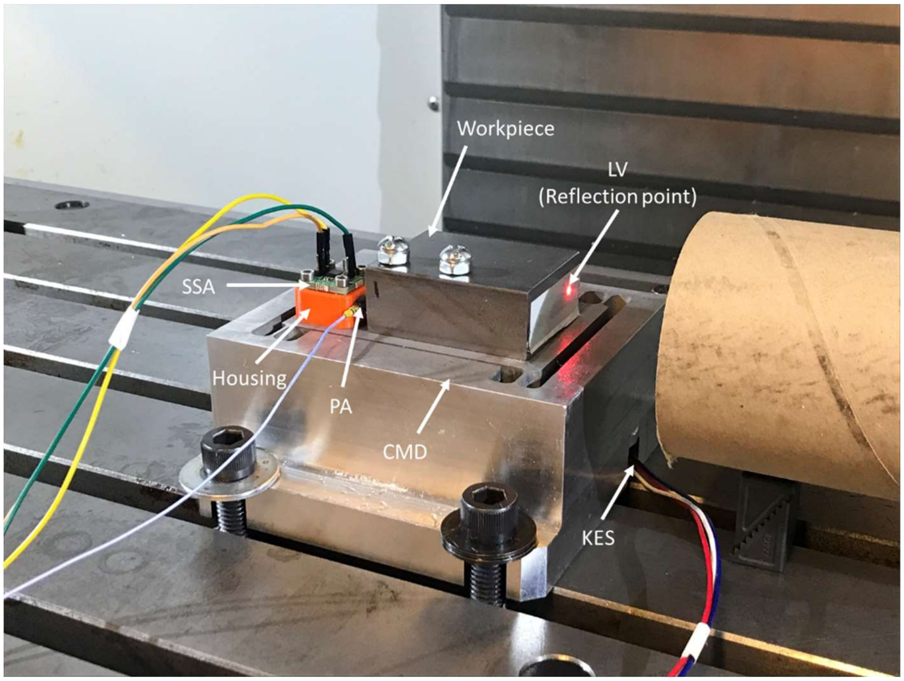

Figure 3.1. Setup of the CMD, showing the workpiece, housing, SSA, PA, LV (reflection point), and the KES.

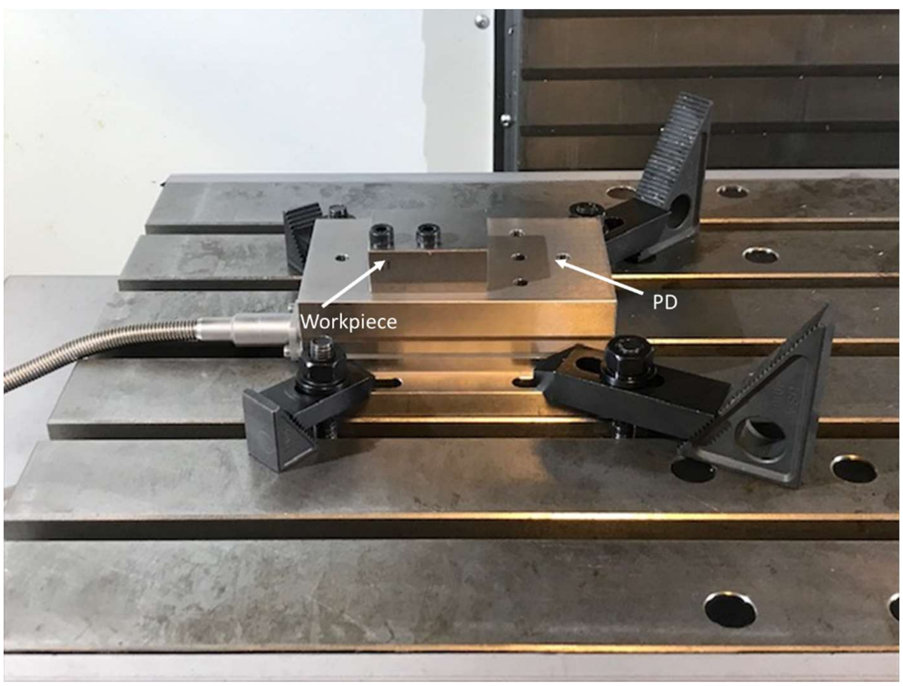

Figure 3.2. PD in the machine with attached workpiece.

Procedure

After the setup was complete, tool tip and workpiece FRFs were measured by tap testing. The tool tip FRFs were measured in both the machine x direction and y direction using a modal hammer (PCB Piezotronics 086C02 ICP ® Impact Hammer) and the PA. Because the CMD only has a single degree of freedom, the workpiece FRF was only measured in the x-direction, with the PA attached directly to the workpiece. For the PD, the workpiece FRFs were measured in both the x-direction and y-direction, with the PA attached to the workpiece, as it is sensitive in both directions.

These FRFs were used together with the 1018 steel workpiece material cutting force model to general stability maps. The stability maps were used to select cutting conditions that provided stable (chatter-free) machining conditions. Because the CMD was more flexible than the PD, the milling parameters were selected using the CMD and tool tip FRFs. The stability map is displayed in Figure 3.3. The figure shows that an axial depth of 2 mm and spindle speed of 5900 rpm stable behavior is predicted. The down milling radial depth for this figure is 4 mm.

Next, the CMD workpiece FRF was measured using the KES, LV, and SSA. This step was repeated after each pair of x-direction and y direction cuts, where the feed per tooth was changed after a set of cuts. These FRFs were used to convert the measured displacement (KES), velocity (LV), and acceleration (SSA and PA) signals to force as described in Chapter 4.

Similarly, for the PD, force-to-force FRFs were measured using the PD's output force and the input force from the modal hammer. The force-to-force FRFs were measured in the machine x direction and y direction. This step was also repeated after each feed per tooth. These force-to-force FRFs were used to filter the measured force and remove the effects of the PD dynamics. Results are shown in Chapter 4.

The experimental cutting forces were obtained using the cutting parameters in Table 3.1. The tool used was a CoroMill® 390 19.05 mm diameter indexable mill with a single insert (390R-070204E-MM S30T), creating a single tooth cutting tool.

For the CMD, sequential cuts in both the x-direction and y-direction were taken at each feed per tooth. As the CMD has only a single degree of freedom, the y-direction cutting forces were obtained by feeding the tool in the y-direction and determining the corresponding x direction forces, which represent the y-direction forces for a feed in the x-direction. The PD is capable of measuring both x direction and y direction forces, so the y direction forces were measured directly from a single cut with a feed in the x direction.

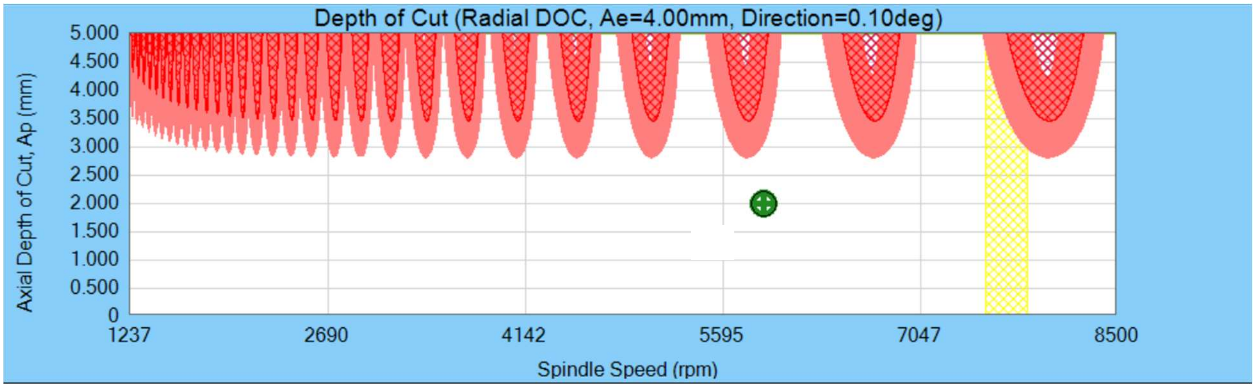

Figure 3.3 Stability map generated from the CMD and tool tip FRFs. The green dot shows a stable cut is possible at a spindle speed of 5900 rpm and an axial depth of cut of 2 mm for down milling at a 4 mm radial depth of cut.

Table 3.1. Cutting parameters

Cutting parameter	Value
Spindle speed	5900 rpm
Tool diameter	19.05 mm
Milling direction	Down milling
Axial depth of cut	2 mm
Radial depth of cut	4 mm
Feed per tooth	
Run 1	0.075 mm/tooth
Run 2	0.100 mm/tooth
Run 3	0.125 mm/tooth
Run 4	0.150 mm/tooth

CHAPTER 4: DATA ANALYSIS

The following data analyses were performed for the displacement, velocity, and acceleration sensors. The x-direction milling cuts used for the data analysis examples were completed using the following conditions: feed per tooth of 0.075 mm/tooth, axial depth of 2 mm, radial depth of 4 mm, spindle speed of 5900 rpm, and down milling.

Knife Edge Sensor (KES)

The data analysis for the KES is provided here. To begin the analysis, the signal offset from zero (i.e., DC offset) had to be removed by selecting a portion of the signal before the tool entered the workpiece and calculating its mean. The mean value was then subtracted from the entire signal, effectively removing the DC offset. A comparison between the measured signal and the signal with the offset removed can be seen in Figure 4.1, and the displacement with the DC offset removed can be seen in Figure 4.2. Once the DC offset was removed, a steady state portion of the signal was extracted. In this case, a five second sample was taken between four and nine seconds. The extracted steady state portion of the signal can be seen in Figure 4.3, and a further close up of the steady state portion is shown in Figure 4.4. Note that this signal includes both a mean value and dynamic variations (i.e., both DC and AC components).

Next, the time domain displacement signal was transformed into the frequency domain using the fast Fourier transform (FFT). The resulting frequency spectrum can be seen in Figure 4.5. The first spike in the signal after the zero-frequency content occurs at the tooth passing frequency, which for this case was 5900 rpm/60 sec/min = 98.3 Hz, and the remaining spikes occur at harmonics (multiples) of the tooth passing frequency.

The frequency domain displacement was converted to frequency domain milling force using the frequency response function (FRF) for the constrained motion dynamometer (CMD). The CMD FRF was measured using a tap test (i.e., a modal hammer was used to excite the CMD in the x direction and the x response was measured using the KES). The resulting FRF was in the form of a receptance, meaning it was in the form of displacement over force, as seen in Figure 4.6. The receptance was then inverted to give the dynamic stiffness, or the force over displacement. As shown in Equation 32, multiplication in the frequency domain of the measured displacement with the dynamic stiffness yields the milling force in the x (feed) direction.

$$F_x = X\frac{F_x}{X} \tag{32}$$

Due to the increase in dynamic stiffness at high frequencies, multiplication by the dynamic stiffness amplifies high frequency content in the displacement. To compensate for this amplification and remove the corresponding noise effects, a third order, lowpass, Butterworth filter with a cutoff frequency of 750 Hz was applied; this cutoff frequency value was selected to be above the desired content at the tooth passing frequency and its first few harmonics and just higher than the CMD natural frequency (approximately 720 Hz). As seen in Figure 4.6, the filter has the effect of rolling off the high frequency portion of the dynamic stiffness, so that when the

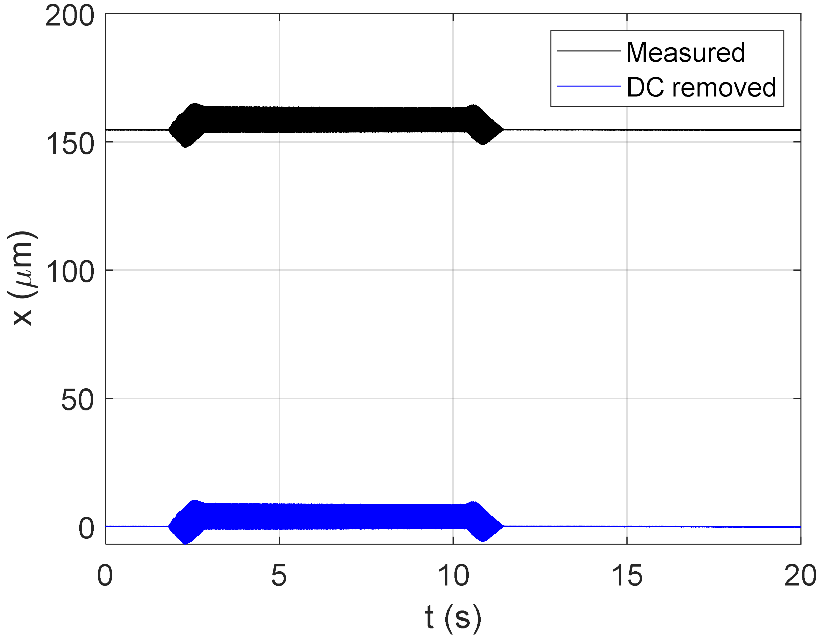

Figure 4.1. Comparison of the measured displacement signal to the measured signal with the DC offset removed.

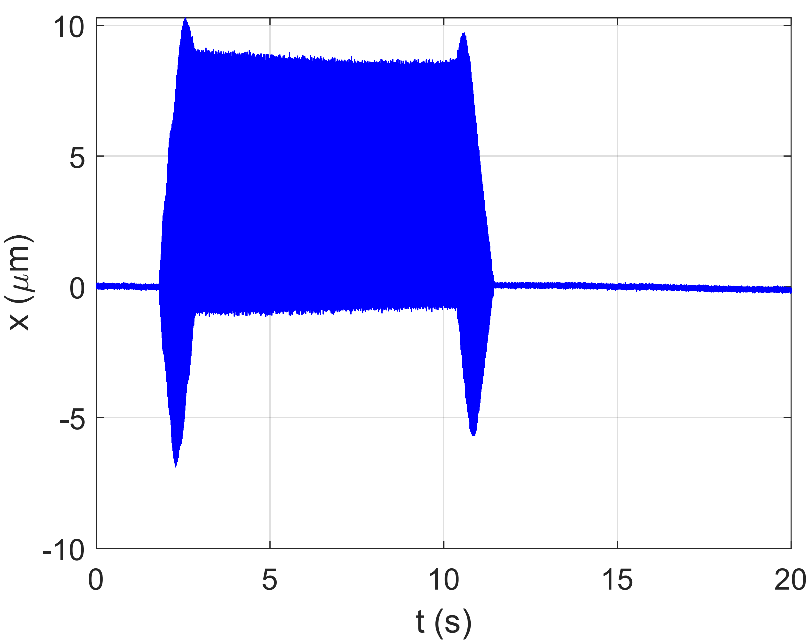

Figure 4.2. The displacement as measured by the KES with the DC offset removed. The KES signal includes both mean and dynamic content.

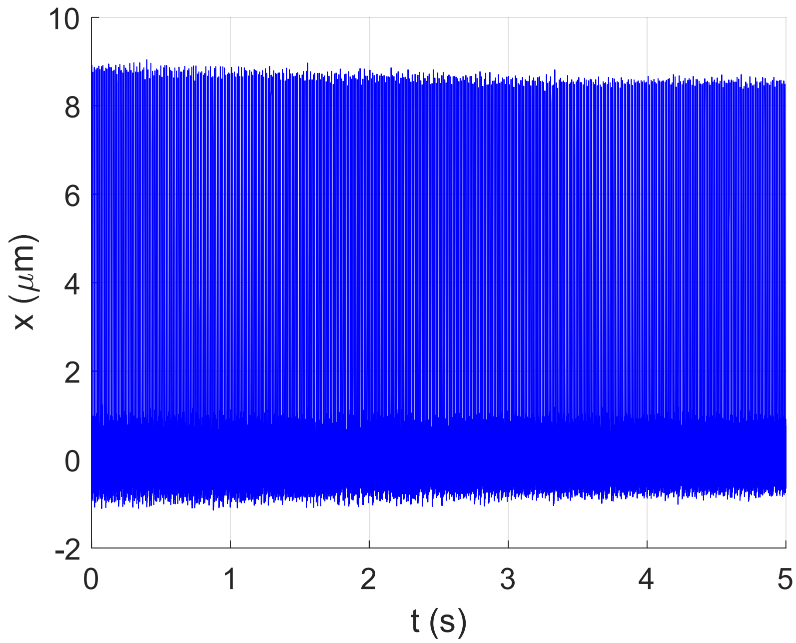

Figure 4.3. Steady state portion of the displacement signal measured by the KES

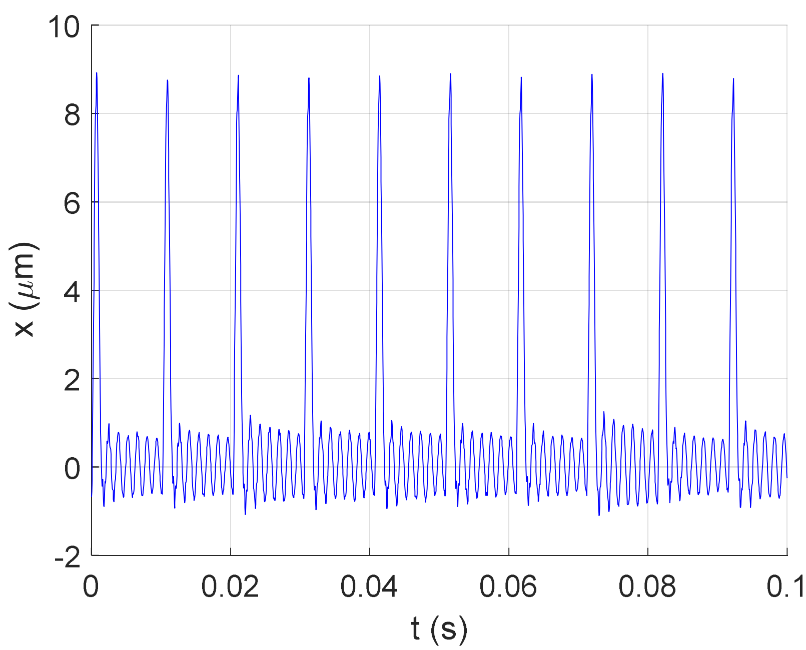

Figure 4.4. Close up of the steady state portion of the displacement as measured by the KES.

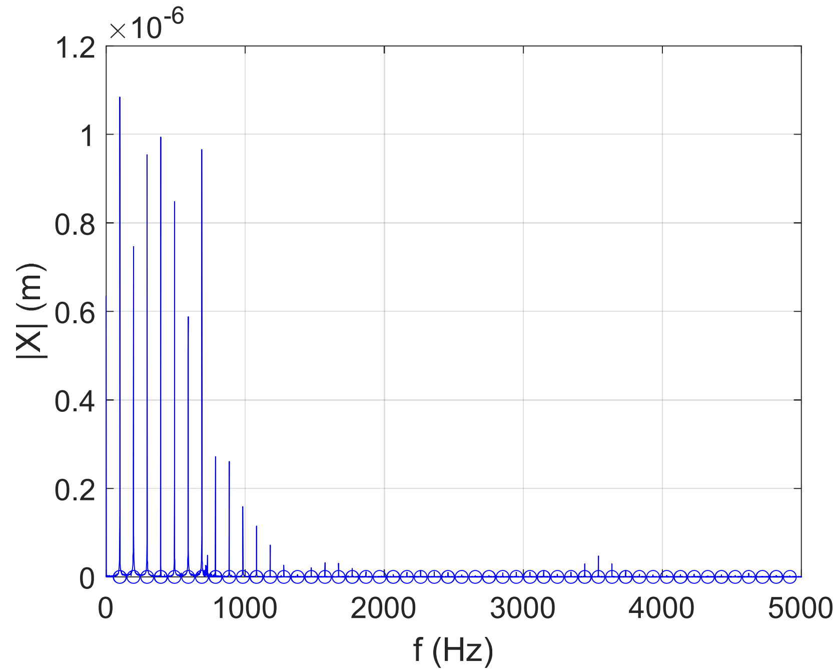

Figure 4.5. Frequency spectrum of the steady state displacement measured by the KES.

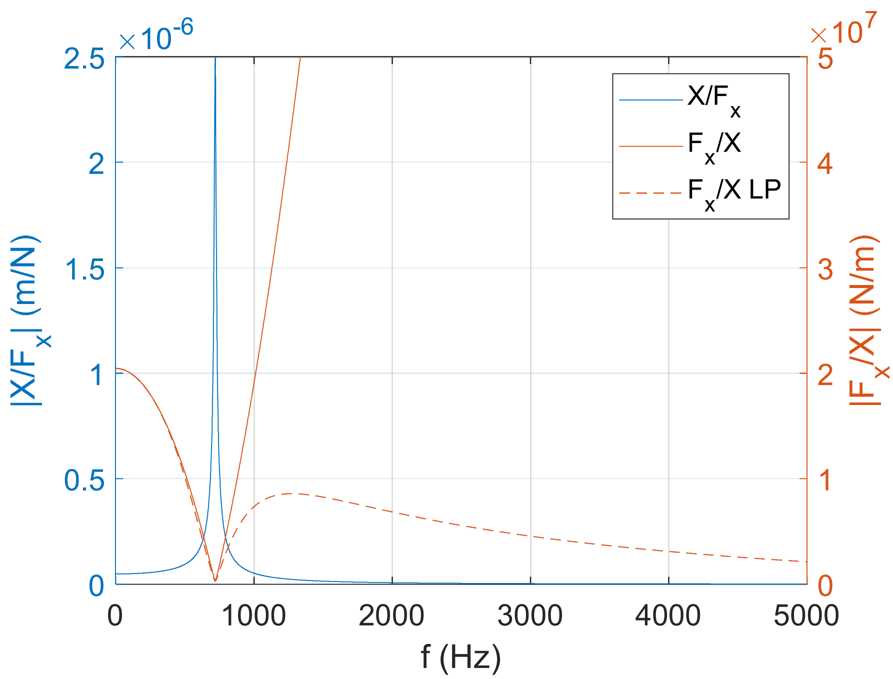

Figure 4.6. The receptance (X/F_x), dynamic stiffness (F_x/X), and lowpass (LP) filtered dynamic stiffness as measured by the KES.

filtered dynamic stiffness is multiplied with the displacement signal, the resulting high frequency force data is attenuated.

The frequency domain force resulting from the multiplication of the frequency domain displacement signal with the lowpass filtered dynamic stiffness can be seen in Figure 4.7. Once the frequency domain force was obtained, the new force signal was converted back to the time domain using the inverse FFT. An example of the resulting time domain force can be seen in Figure 4.8. A single tooth passage was then selected for comparison with forces determined from the commercially-available piezoelectric dynamometer (PD) and time domain simulation (TDS). The comparison can be seen in Figure 4.9. Good agreement is observed.

Laser Vibrometer (LV)

The data analysis for the LV is provided here. To begin, the DC offset had to be removed. This was done by selecting a portion of the signal before the tool entered the workpiece and taking the mean of that portion. The mean value was then subtracted from the entire signal, effectively removing the DC offset. As the LV was not mounted to the table with the workpiece, the instrument measured the machine's table velocity as well as the velocity of the workpiece (mounted to the CMD) during milling. In this case, the table velocity was taken to be the DC offset. A comparison between the measured velocity signal and the signal with the offset removed can be seen in Figure 4.10. The velocity of the workpiece with the DC offset removed can be seen in Figure 4.11. A steady state portion of the signal was then extracted and can be seen in Figure 4.12. A smaller sample of the steady state portion can be seen in Figure 4.13.

Next, the time domain velocity signal was transformed into the frequency domain using the FFT. Unlike the KES case, the mean value of the steady state signal is zero for the LV. The resulting frequency spectrum can be seen in Figure 4.14. The first peak occurs at the tooth passing frequency, which for this case was 98.3 Hz, and the remaining spikes occur at harmonics of the tooth passing frequency.

As with the KES, the frequency domain velocity was converted to frequency domain milling force using the frequency response function (FRF) for the constrained motion dynamometer (CMD). Because the LV measures velocity, the mobility was needed to convert the velocity signal to force. The mobility can be obtained from the receptance by differentiation, which in the frequency domain is performed by multiplying the receptance by $i\omega$ as seen in Equation 33, where i is the imaginary variable and ω is frequency.

$$\frac{V_x}{F_x} = i\omega \, \frac{X}{F_x} \tag{33}$$

The resulting FRF can be seen in Figure 4.15. The mobility was then inverted to give the mechanical impedance, or the force over velocity. Multiplication in the frequency domain of the measured velocity with the mechanical impedance yields force, as shown in Equation 34.

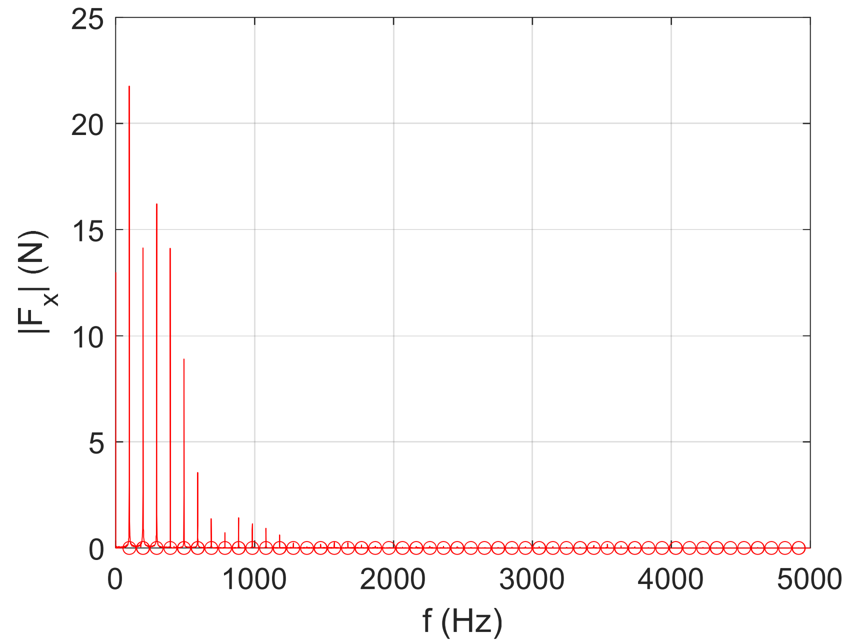

Figure 4.7. The frequency spectrum of the force, as determined by the KES.

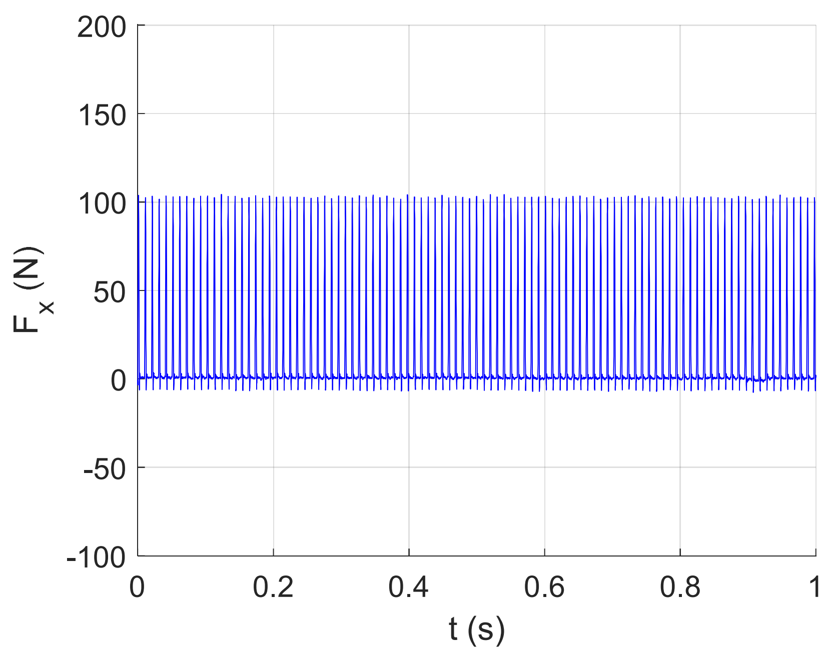

Figure 4.8. Sample of the force as determined by the KES.

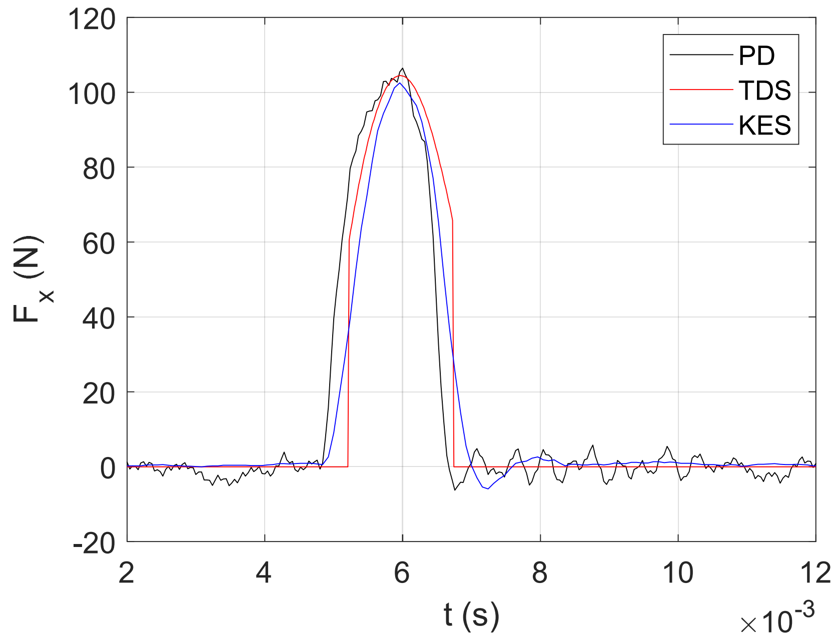

Figure 4.9. Comparison of the force for a single tooth passing as determined by the PD, TDS, and the KES. Good agreement is observed.

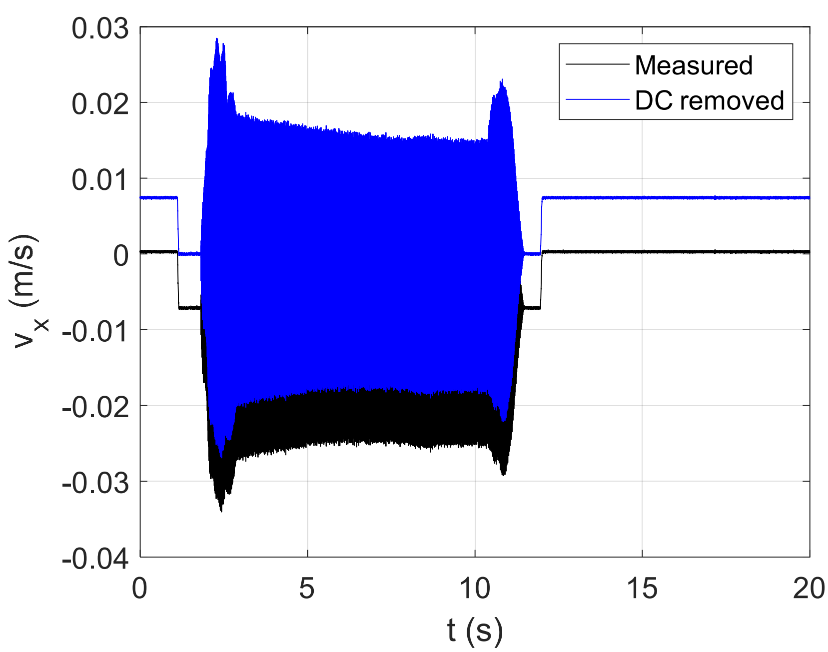

Figure 4.10. Comparison of the measured velocity signal to the measured signal with the DC offset removed.

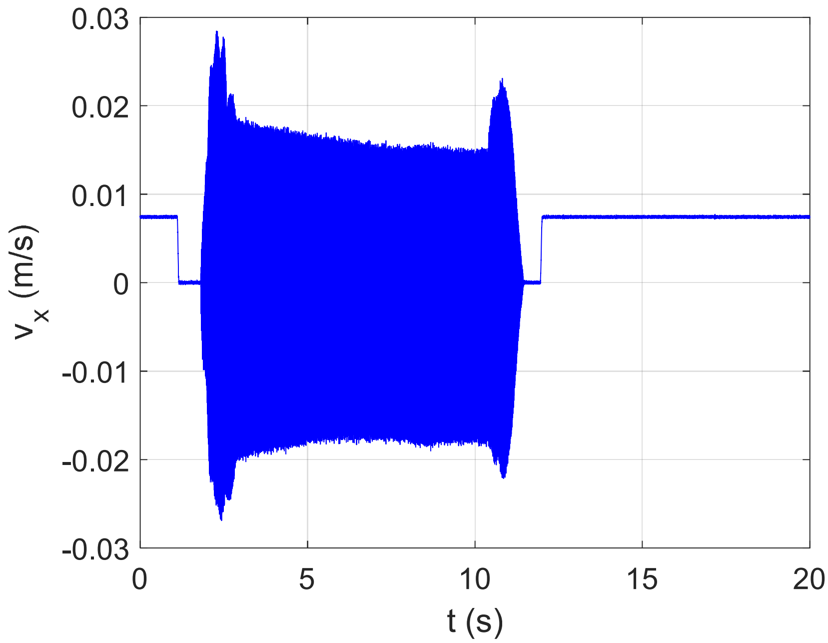

Figure 4.11. Velocity of the workpiece with the DC offset removed

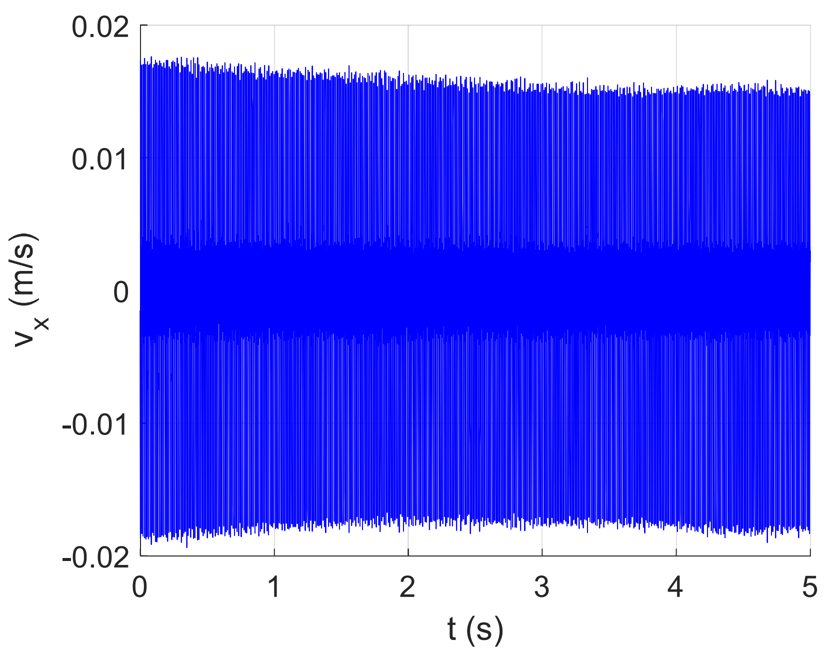

Figure 4.12. Steady state portion of the velocity signal measured by the LV.

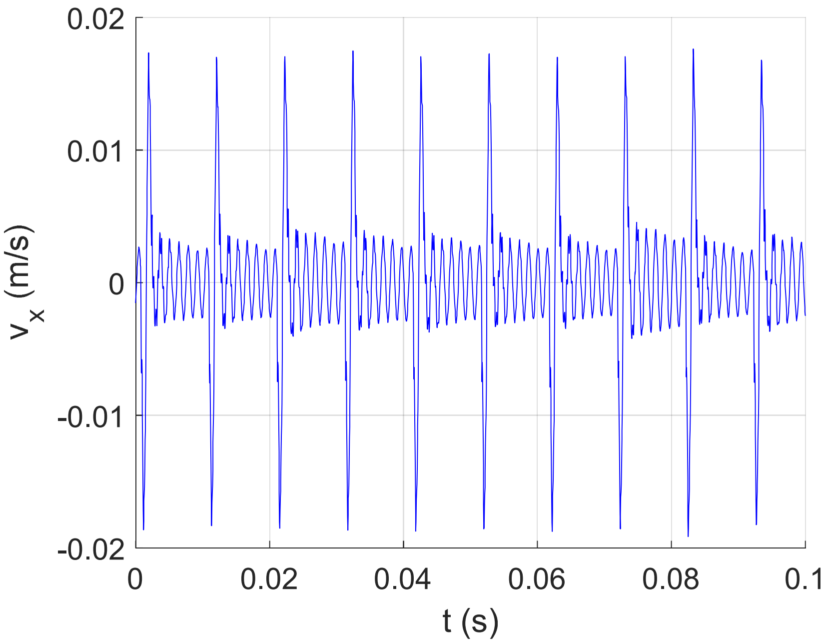

Figure 4.13 Close up of the steady state portion of the velocity as measured by the LV.

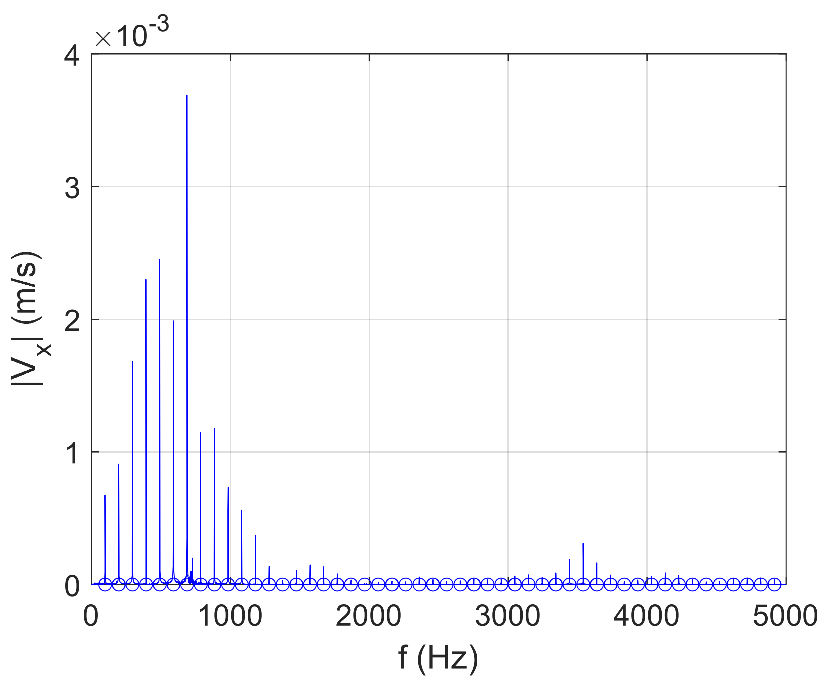

Figure 4.14. Frequency spectrum of the steady state velocity measured by the LV.

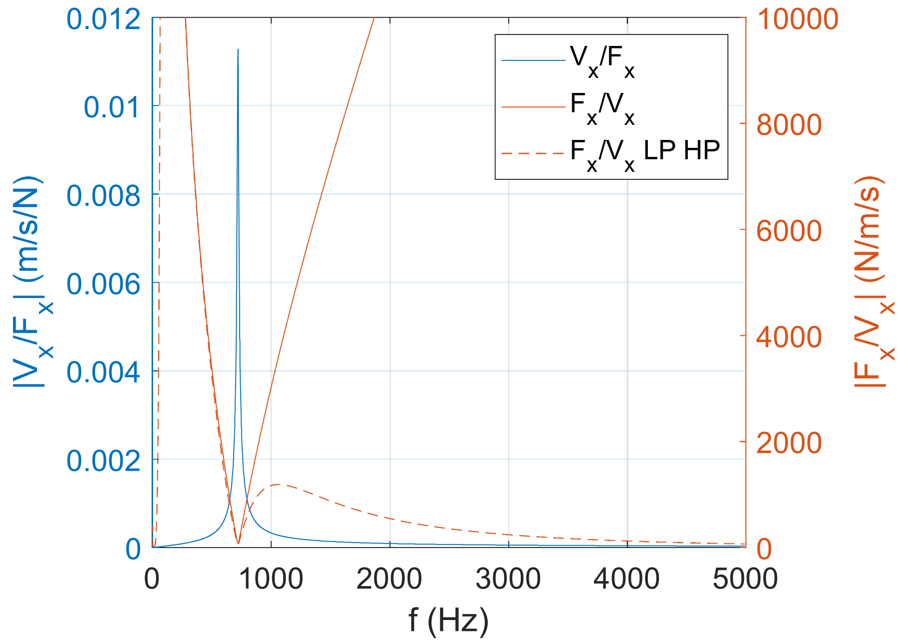

Figure 4.15 The mobility (V_x/F_x), mechanical impedance (F_x/V_x), and lowpass/highpass filtered mechanical impedance as measured by the LV.

$$F_x = V_x \frac{F_x}{V_x} \tag{34}$$

Multiplication by the mechanical impedance amplifies both low and high frequency content. To compensate for this, the mechanical impedance was multiplied by both lowpass and high-pass filters, or in other words, the mechanical impedance was multiplied by a low-pass and high-pass filter. The lowpass filter was a third order Butterworth filter with a cutoff frequency of 750 Hz. The high pass filter was a sixth order Butterworth filter with a cutoff frequency of 83 Hz; this value was selected to be below the tooth passing frequency of 98.3 Hz to avoid attenuating the desired content at this frequency. As seen in Figure 4.15, the filters have the effect of rolling off the low and high frequency portions of mechanical impedance, so that when the filtered mechanical impedance is multiplied with the velocity signal, the resulting low and high frequency force data are attenuated. The frequency domain force resulting from the multiplication of the frequency domain velocity signal with the filtered mechanical impedance can be seen in Figure 4.16.

Once the frequency domain force was obtained, the new force signal was converted back to the time domain using the inverse FFT. A sample of the time domain force signal as determined by the LV can be seen in Figure 4.17. A single tooth passing was then selected for comparison with forces determined from the PD and TDS. The comparison can be seen in Figure 4.18. The agreement is not as good as the KES and the mean component of the force is lost by the LV. This is because the signal mean value is zero, unlike the KES which retained the mean value through the frequency domain analysis.

Solid State Accelerometer (SSA)

The data analysis for the SSA is provided here. Analysis for the piezoelectric accelerometer (PA) is identical, so it is not covered separately. To begin, the DC offset had to be removed. This was done by selecting a portion of the signal before the tool entered the workpiece and taking the mean of that portion. The mean value was then subtracted from the entire signal, effectively removing the DC offset. Note that the mean of the corresponding signal is zero. This is the same as the LV, but different than the KES. The results of removing the offset in comparison to the measured signal can be seen in Figure 4.19; Figure 4.20 shows just the acceleration as measured by the SSA with the DC offset removed. Once the DC offset was removed, a steady state portion of the signal was extracted. In this case, a five second sample was taken between four and nine seconds. Figure 4.21 shows the steady state portion of the acceleration signal as measured by the SSA, and a close up of the steady state portion of the acceleration can be seen in Figure 4.22.

Next, the time domain acceleration signal was transformed into the frequency domain using the FFT. As with the LV, the mean value of the signal was zero. The resulting frequency spectrum can be seen in Figure 4.23. The first spike in the signal after the zero frequency occurs at the tooth passing frequency, which for this case was 98.3 Hz, and the remaining spikes occur at harmonics of the tooth passing frequency.

As with the KES and LV, the frequency domain acceleration was converted to frequency domain milling force using the frequency response function (FRF) for the constrained motion dynamometer (CMD).

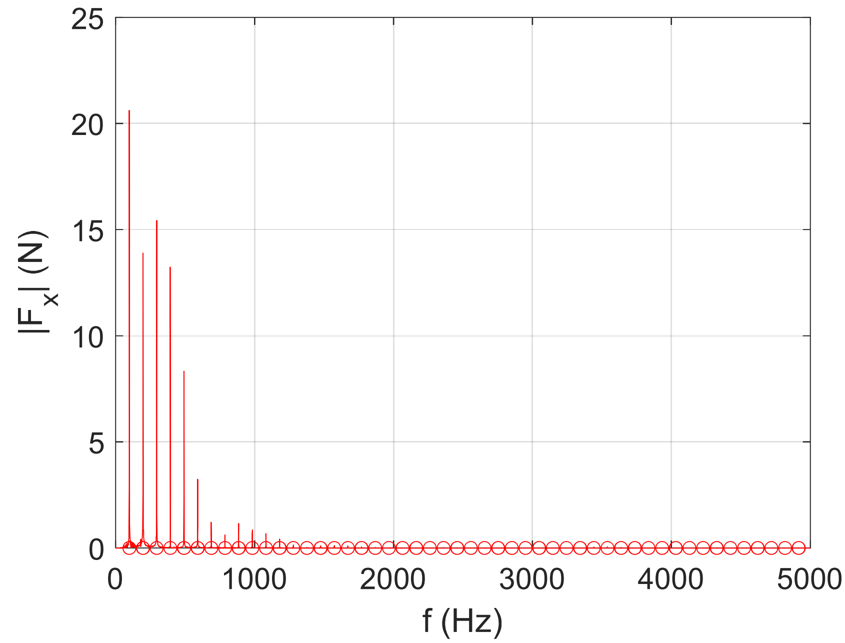

Figure 4.16. Frequency spectrum of the force as determined by the LV.

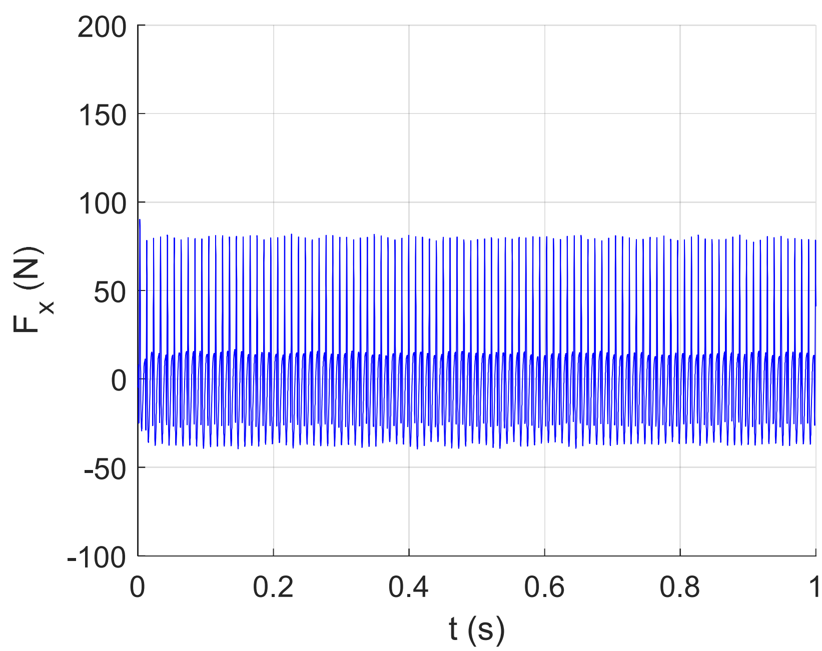

Figure 4.17. Sample of the force as determined by the LV.

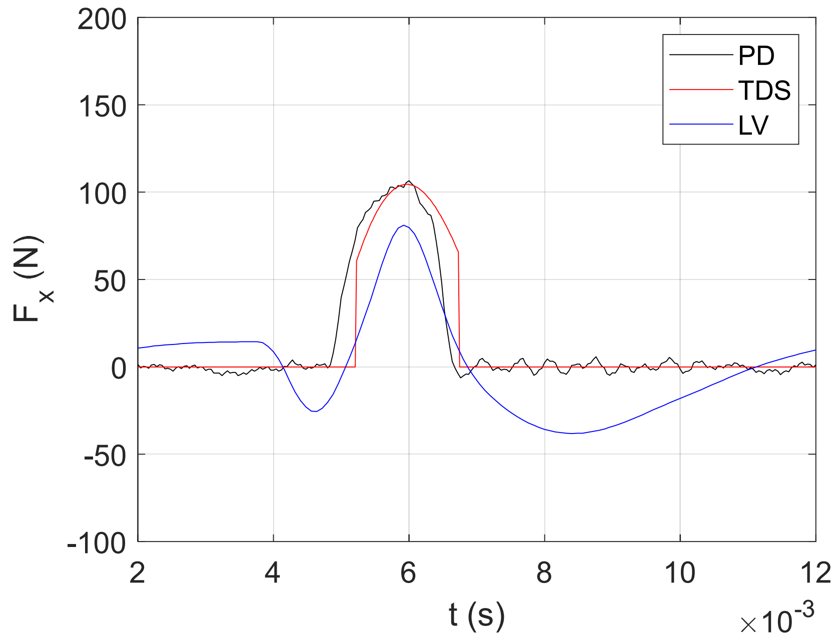

Figure 4.18. Comparison of the force for a single tooth passing as determined by the PD, the TDS, and the LV. The agreement is not as good as the KES and the mean value of the force is lost.

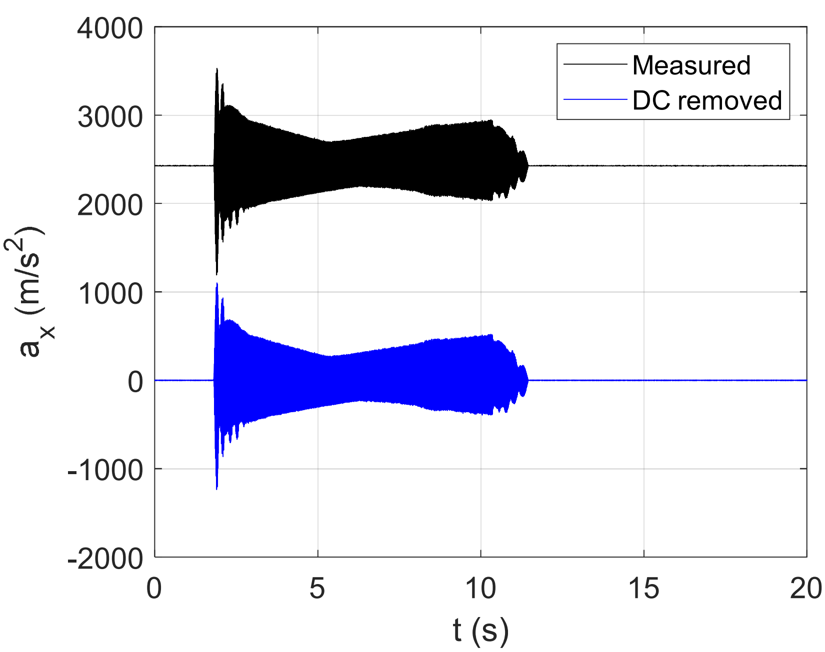

Figure 4.19. Comparison of the measured acceleration signal to the measured signal with the DC offset removed, as measured by the SSA.

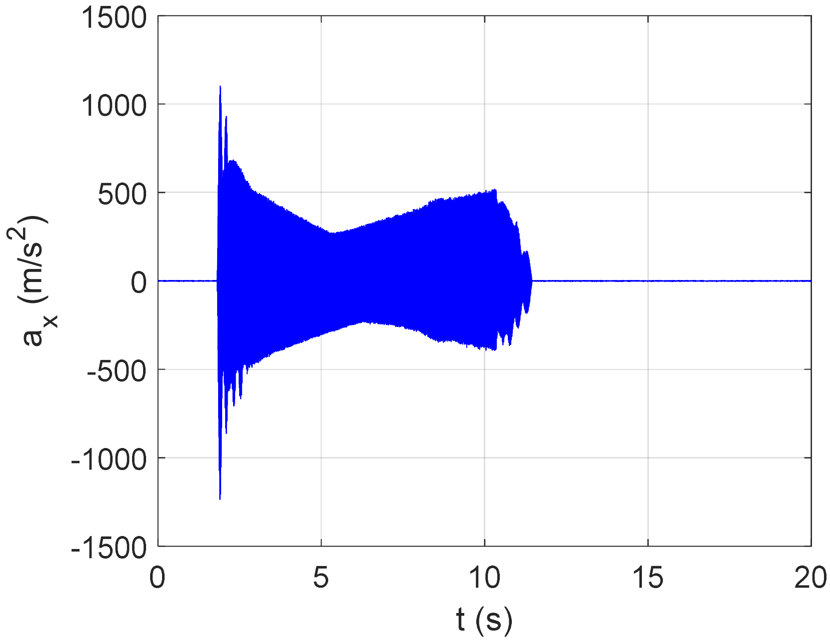

Figure 4.20. Acceleration as measured by the SSA with the DC offset removed.

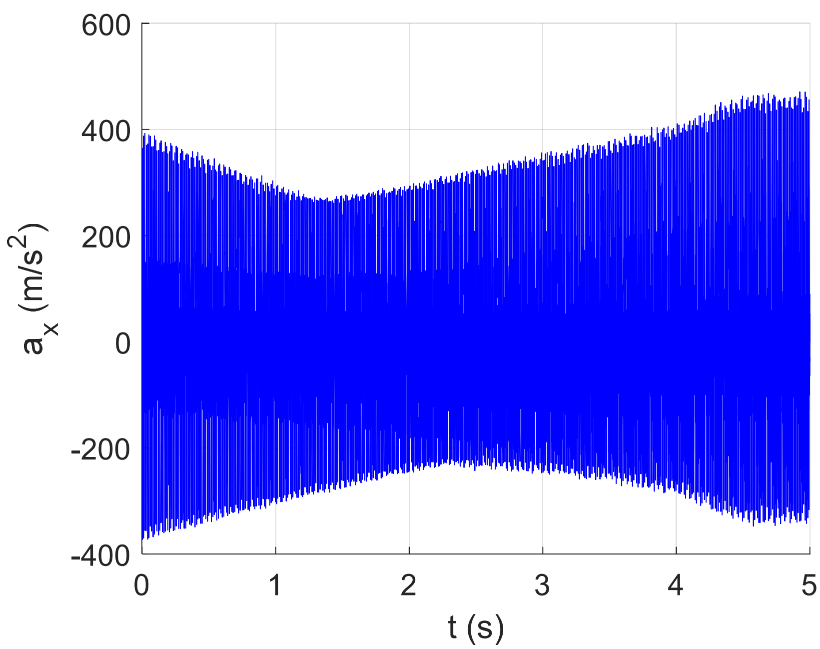

Figure 4.21. Steady state portion of the acceleration signal measured by the SSA.

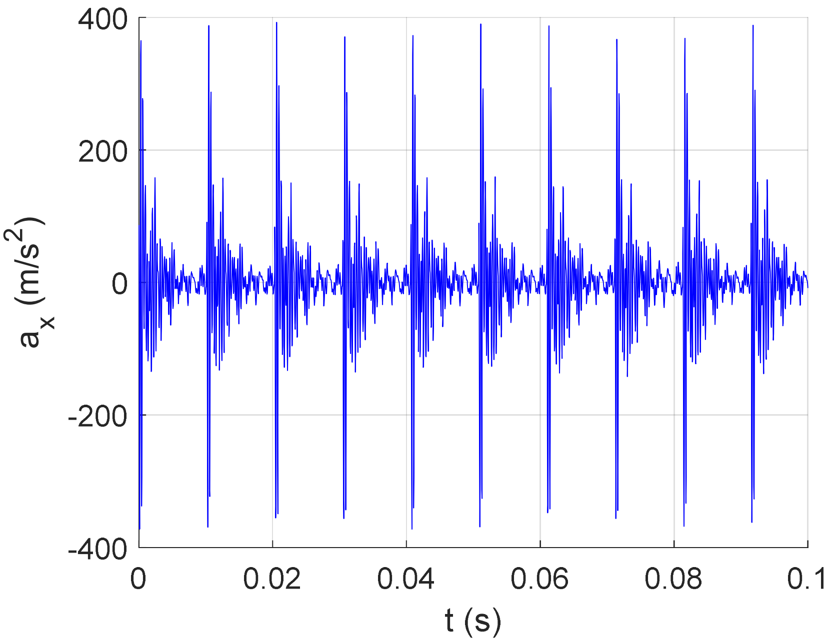

Figure 4.22. Close up of the extracted steady state acceleration.

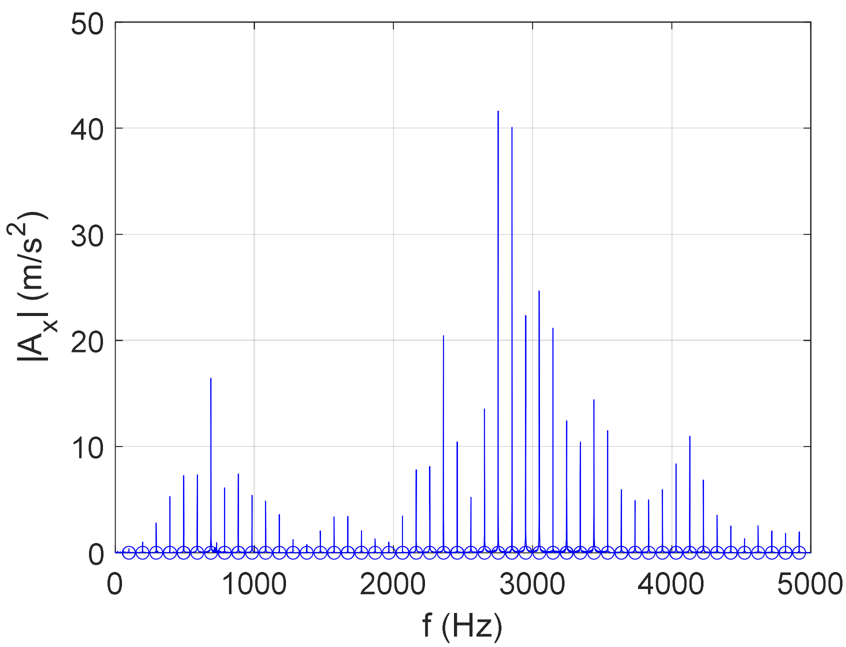

Figure 4.23. Frequency spectrum of the steady state acceleration signal.

Because the SSA measures acceleration, the accelerance is needed to convert the acceleration signal to force. Accelerance can be obtained from the receptance by twice differentiation, which in the frequency domain can be completed by multiplying the receptance by $-\omega^2$ as seen in Equation 35.

$$\frac{A_x}{F_x} = -\omega^2 \frac{X}{F_x} \tag{35}$$

The resulting FRF can be seen Figure 4.24. The accelerance was then inverted to give the dynamic mass, or the force over acceleration. Multiplication in the frequency domain of the measured acceleration with the dynamic mass yields force, as shown in Equation 36.

$$F_x = A_x \frac{F_x}{A_x} \tag{36}$$

However, multiplication by the dynamic mass amplifies low frequency content. To compensate for this, the accelerance was multiplied by a highpass filter. A lowpass filter was also included to attenuate the high frequency noise in the accelerometer signal. The lowpass filter was a third order Butterworth filter with a cutoff frequency of 750 Hz. The highpass filter was a sixth order Butterworth filter with a cutoff frequency of 83 Hz. As seen in Figure 4.24, the filters have the effect of rolling off the low and high frequency portion of the dynamic mass, so that when the filtered dynamic mass is multiplied by the acceleration signal, the resulting low and high frequency force data are attenuated. The frequency domain force resulting from the multiplication of the frequency domain acceleration signal with the filtered dynamic mass can be seen in Figure 4.25. Once the frequency domain force was obtained, the new force signal was converted back to the time domain using the inverse FFT. A sample of the time domain force signal as determined by the SSA can be seen in Figure 4.26. A single tooth passing was then selected for comparison with forces determined from the PD and TDS. The comparison can be seen in Figure 4.27. The agreement is not as good as the KES and the mean component of the force is lost by the SSA as with the LV. This is because the signal mean value is zero, unlike the KES which retained the mean value through the frequency domain analysis.

Piezoelectric Dynamometer (PD)

The data analysis for the PD is provided here. Because the PD, similar to the CMD, is a dynamic system, its FRF affects the force measurement accuracy. These effects were compensated by measuring the force output to force input, or force-to-force, FRF of the sensor and using the measured FRFs to filter the measured force in the frequency domain. The PD was capable of measuring both *x*-direction and *y*-direction forces simultaneously, thus allowing for the measurement of milling force for both directions for a cut with a single feed direction. Therefore, the force-to force FRFs for both directions were required. The real and imaginary parts of the force-to-force FRF of the PD in the machine *x*-direction and *y*-direction can be seen in Figure 4.28 and Figure 4.29, respectively.

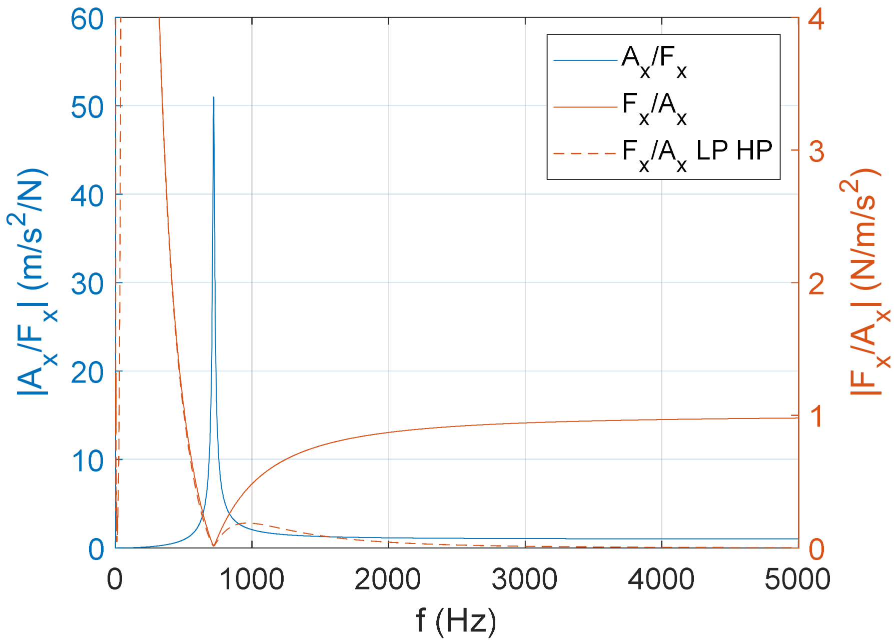

Figure 4.24. Accelerance, dynamic mass, and lowpass (LP) and highpass (HP) filtered dynamic mass.

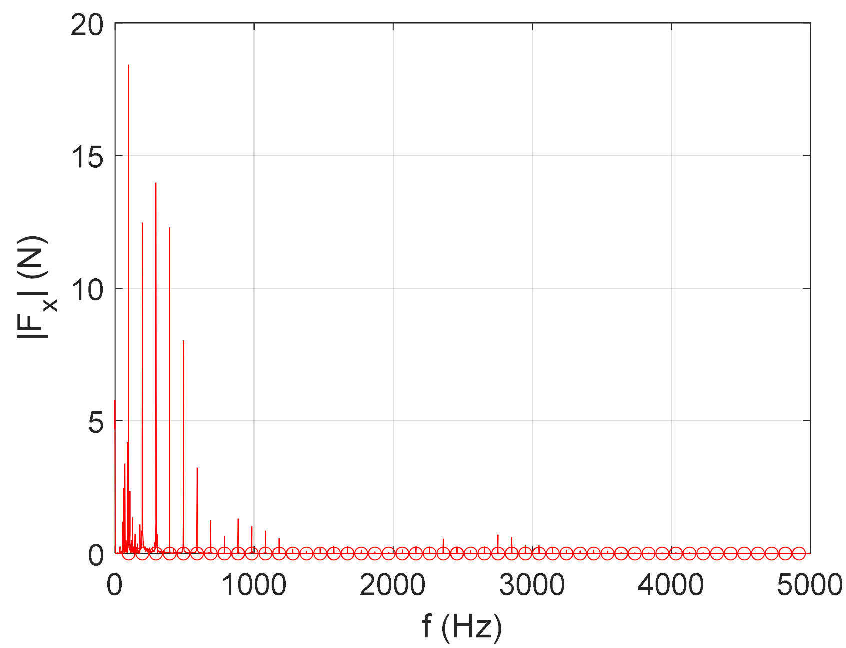

Figure 4.25 Frequency spectrum of the force as determined by the SSA.

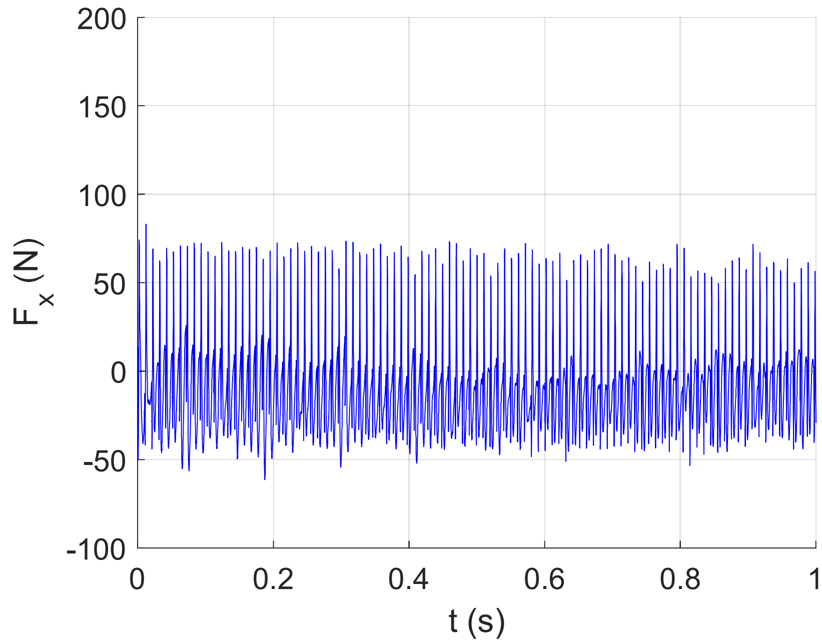

Figure 4.26. A sample of the force as determined by the SSA.

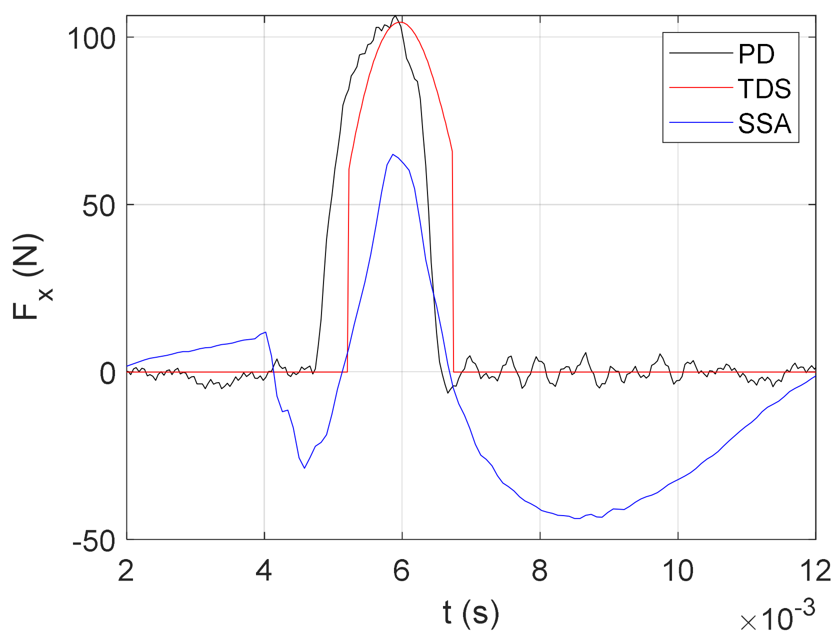

Figure 4.27. Comparison of the force as determined by the PD, TDS, and the SSA. The agreement is not as good as the KES and the mean value is lost.

The force-to-force FRF was then inverted to give a FRF of input force over the measured force. The inverted FRF was then interpolated to match the frequency vector from the FFT on the measured force signals. The interpolated FRFs were multiplied by lowpass third order Butterworth filters with a cutoff frequency of 2000 Hz to attenuate high frequency noise. The magnitude of the inverted force-to-force FRFs and the magnitude of the filtered inverted force-to-force FRFs for both the machine *x*-direction and *y*-direction can be seen in Figure 4.30.

A steady state portion of the time domain force in both the machine x-direction and machine y-direction was selected, and a sample of the steady state forces in both directions can be seen in Figure 4.31. The forces were converted to the frequency domain using the FFT.

Once in the frequency domain, the steady state forces were multiplied by their respective inverted force-to-force FRFs. The multiplication of the frequency domain measured output force by the inverse force-to-force FRF resulted in a filtered force signal as seen in Equation 37.

$$F_{filtered} = F_{measured} \frac{F_{input}}{F_{measured}} \tag{37}$$

The frequency spectrum of the filtered and measured force in the machine *x*-direction can be seen in Figure 4.32. The resulting input forces were then transformed into the time domain using the inverse FFT. The force in the machine x-direction for a single tooth passing can be seen in Figure 4.33.

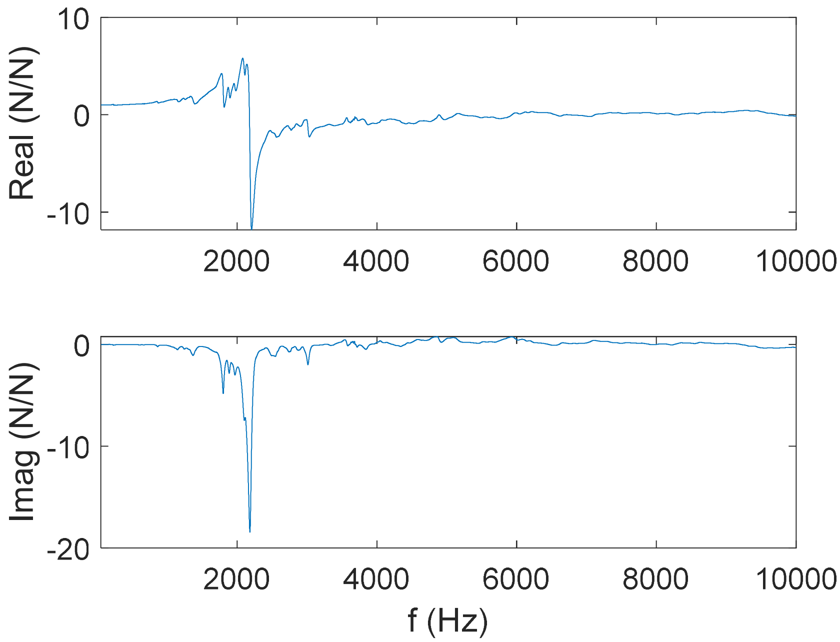

Figure 4.28. Real (top) and imaginary (bottom) force-to-force FRF of the PD in the machine *x*-direction.

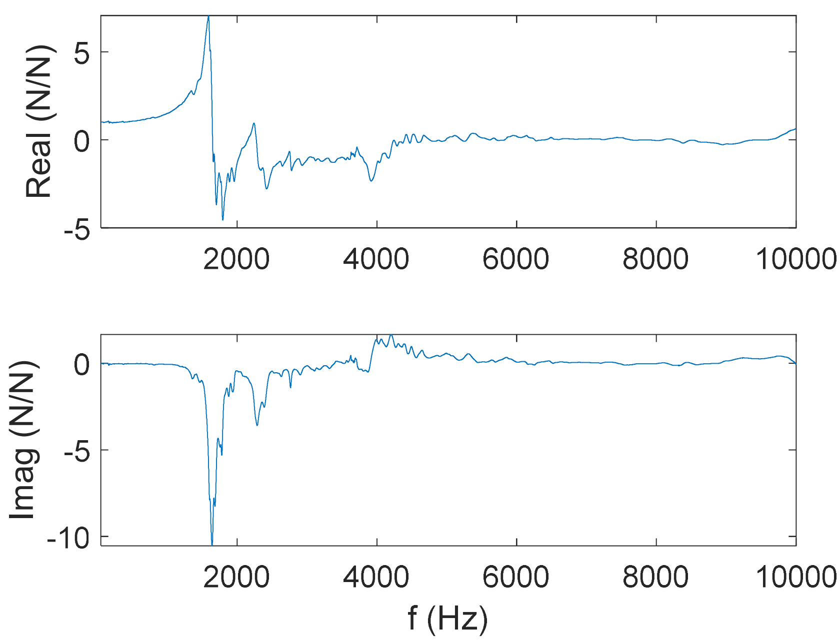

Figure 4.29. Real (top) and imaginary (bottom) force-to-force FRF of the PD in the machine *y*-direction.

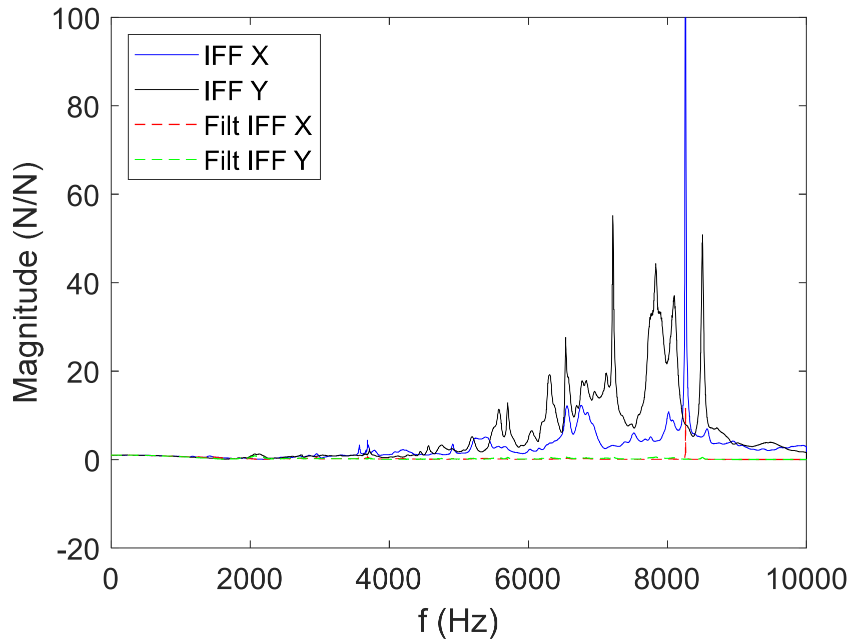

Figure 4.30. Inverted force-to-force (IFF) FRFs and the filtered inverted force-to-force FRFs for the PD in the machine *x*-direction and machine *y*-direction.

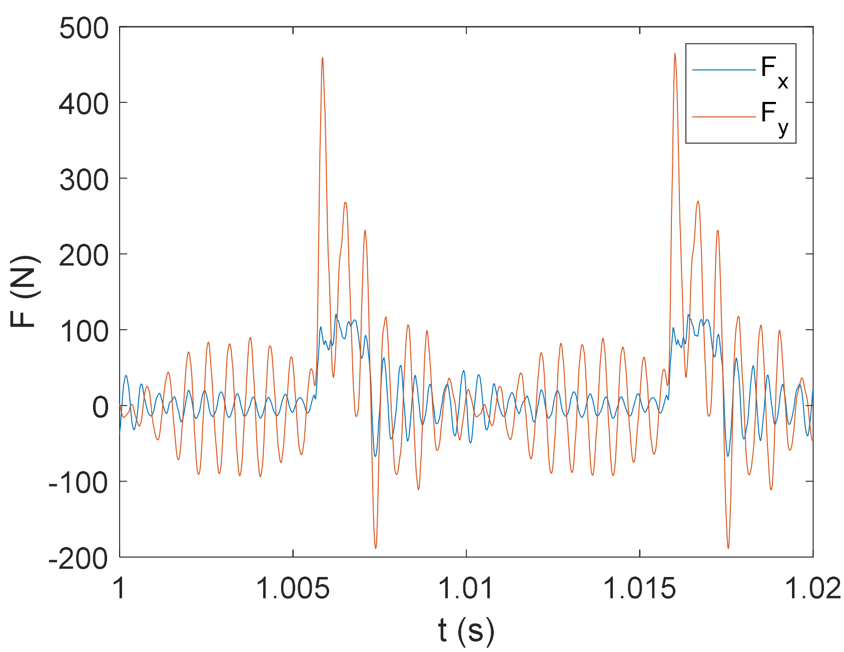

Figure 4.31 Steady state sample of the machine *x*-direction and *y*-direction forces as measured by the PD.

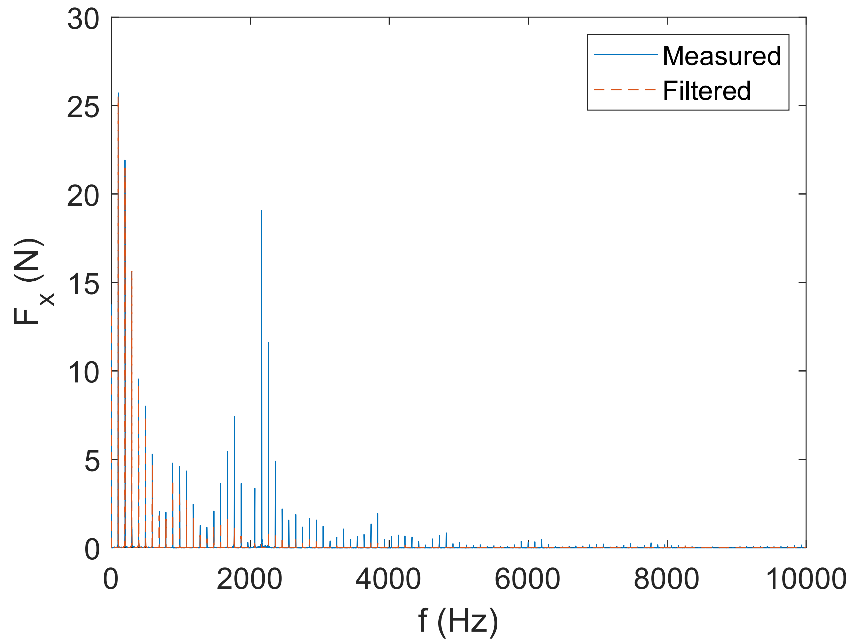

Figure 4.32. Frequency spectrum of the measured and filtered machine *x*-direction forces.

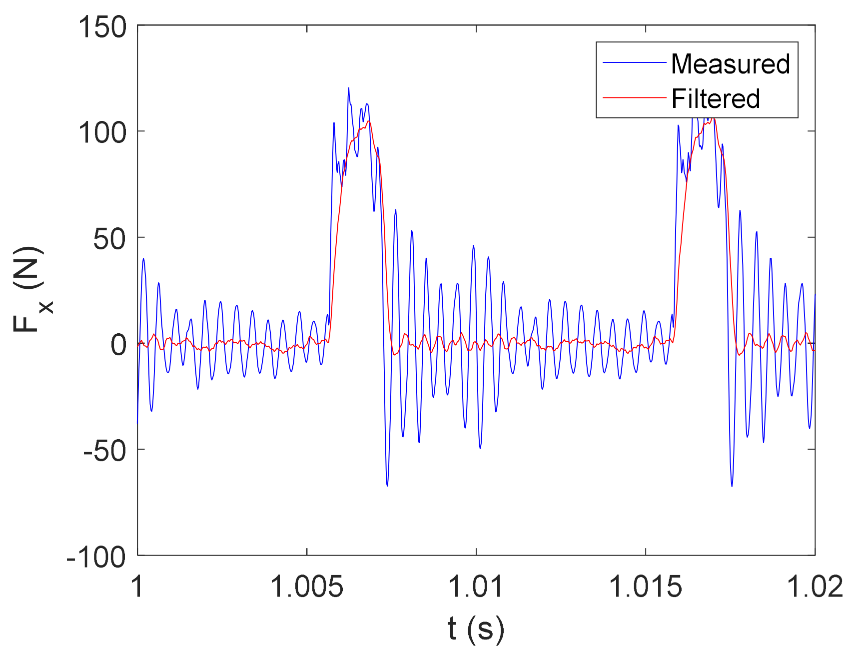

Figure 4.33. Machine *x*-direction measured and filtered forces, as measured by the PD.

CHAPTER 5: RESULTS

Knife Edge Sensor (KES)

In this section, the experimental cutting forces measured by the KES are compared to the forces measured by the piezoelectric dynamometer (PD) as well as to the forces produced by the time domain simulation (TDS). As the CMD has only a single degree of freedom in the machine x-direction, the y-direction forces were obtained by feeding the tool in the y-direction and computing the x-direction forces, which represent the y-direction forces for a feed in the x-direction. The PD is capable of measuring both x-direction and y-direction forces, so the y-direction forces could be obtained directly from a cut with a feed in the x-direction. Similarly, the TDS outputs both the x-direction and y-direction forces for a cut with an x-direction feed.

The x-direction and y-direction forces for a single tooth passing at the four feed per tooth values and other cutting parameters listed in Table 3.1 are shown in Figure 5.1 to Figure 5.8. As seen in the figures, the forces show good agreement between the KES, PD, and TDS. The x-direction and y-direction figures all have the same scales so the increase in force components with larger feed per tooth values can be conveniently observed.

Laser Vibrometer (LV)

In this section, the experimental cutting forces measured by the LV are compared to those of the forces measured by the PD as well as to the forces produced by the TDS. The experimental cutting forces were obtained using the cutting parameters from Table 3.1.

The x-direction and y-direction forces for a single tooth passing at the four feed per tooth values are shown in Figure 5.9 to Figure 5.8. For all of the feeds in both directions, the maximum forces measured by the LV are consistently less than the maximum forces of the PD and TDS. This is due to the mean of the velocity signal being zero; the mean force value is not retained in the LV analysis. To compensate for this, the difference between the maximum and minimum value for a single tooth passage was calculated from the LV data and used to compare to the peak values for the PD and TDS.

Solid State Accelerometer (SSA)

In this section, the experimental cutting forces measured by the SSA are compared to those of the forces measured by the PD as well as to the forces produced by the TDS. The experimental cutting forces were obtained using the cutting parameters Table 5.1.

The x-direction and y-direction forces for a single tooth passing at the four feed per tooth values are shown in Figure 5.17 to Figure 5.24. For all of the feeds in both directions, the maximum forces measured by the SSA are consistently less than the maximum forces of the PD and TDS. This is because mean value of the acceleration signal being zero; the mean value of the force was lost in the SSA data analysis. To compensate for this, the difference between the maximum and minimum values for a single tooth passage was calculated from the SSA data and used to compare to the peak values for the PD and TDS.

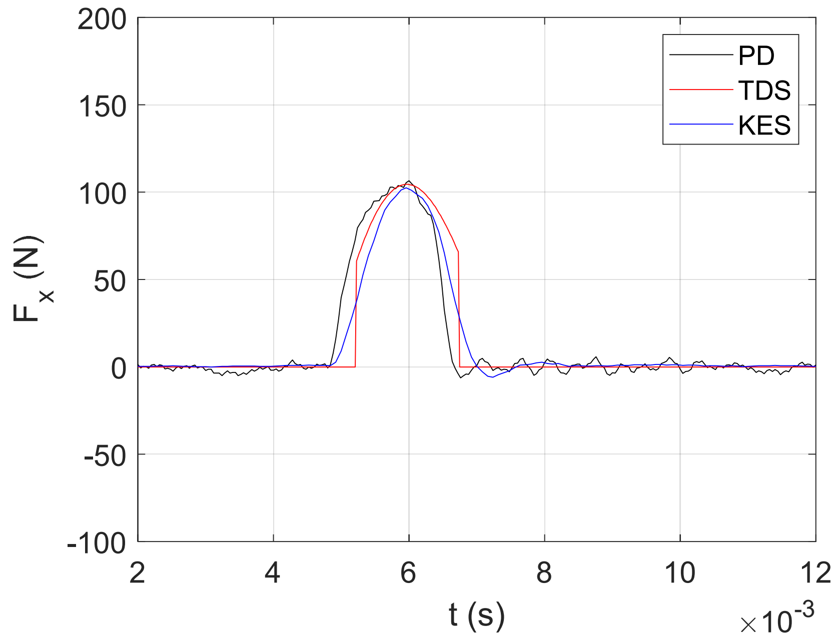

Figure 5.1. *X*-direction force comparison of the PD, TDS, and KES for a single tooth passing at a feed per tooth of 0.075 mm/tooth.

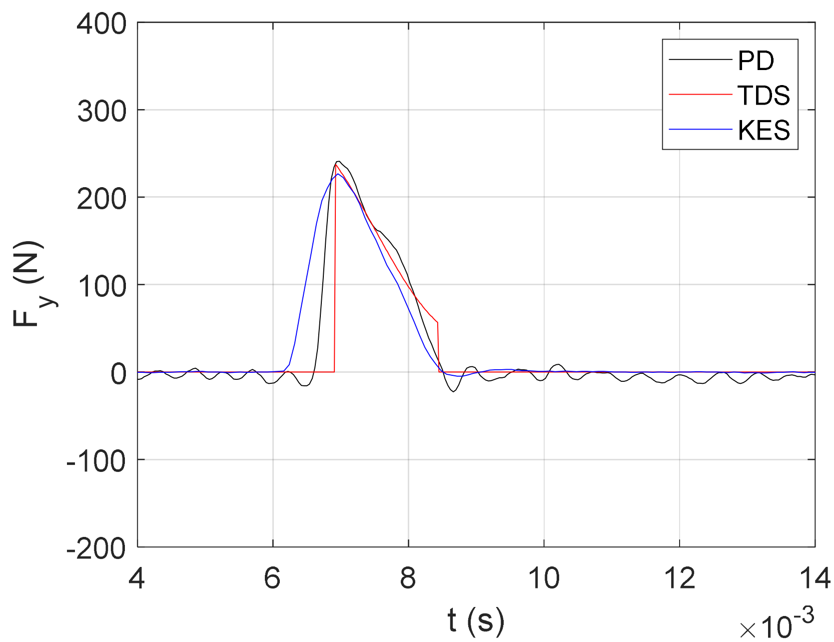

Figure 5.2. *Y*-direction force comparison of the PD, TDS, and KES for a single tooth passing at a feed per tooth of 0.075 mm/tooth

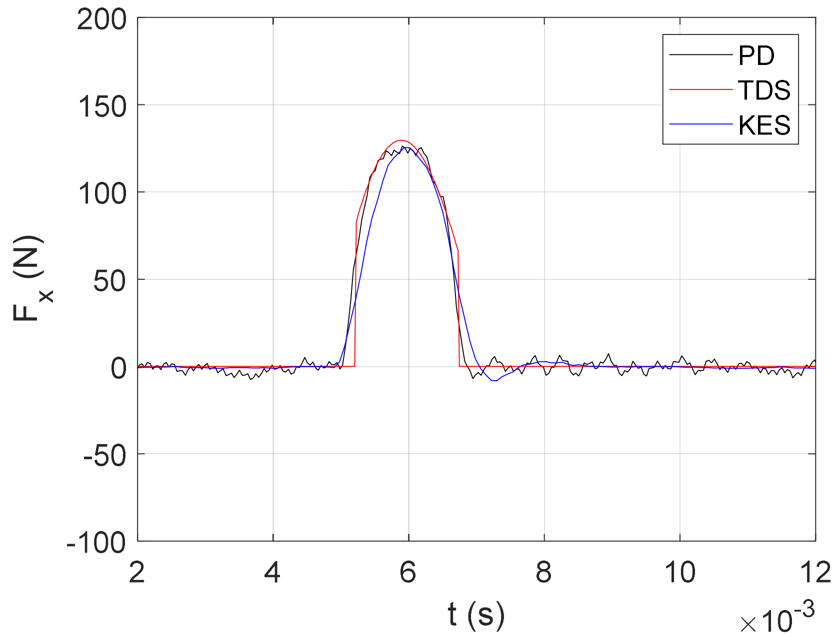

Figure 5.3. *X*-direction force comparison of the PD, TDS, and KES for a single tooth passing at a feed per tooth of 0.100 mm/tooth.

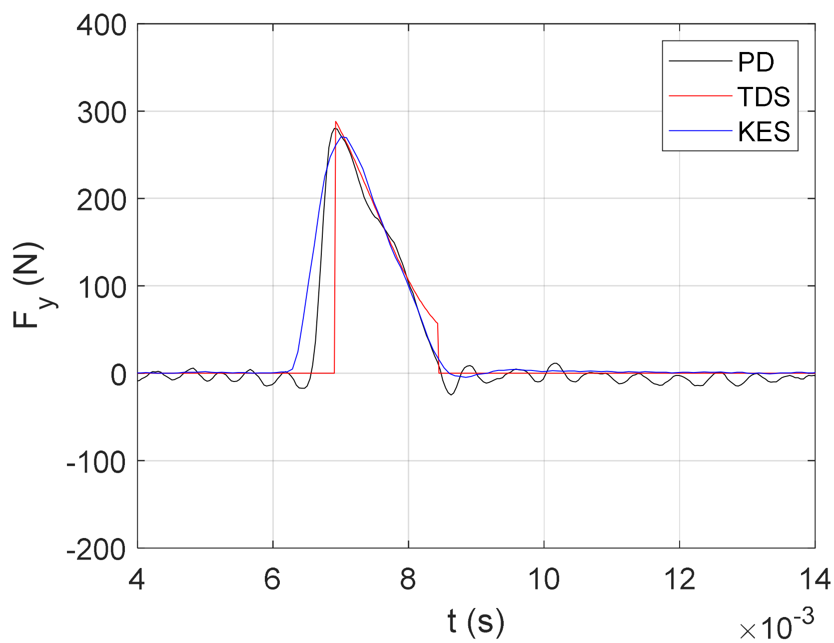

Figure 5.4. *Y*-direction force comparison of the PD, TDS, and KES for a single tooth passing at a feed per tooth of 0.100 mm/tooth.

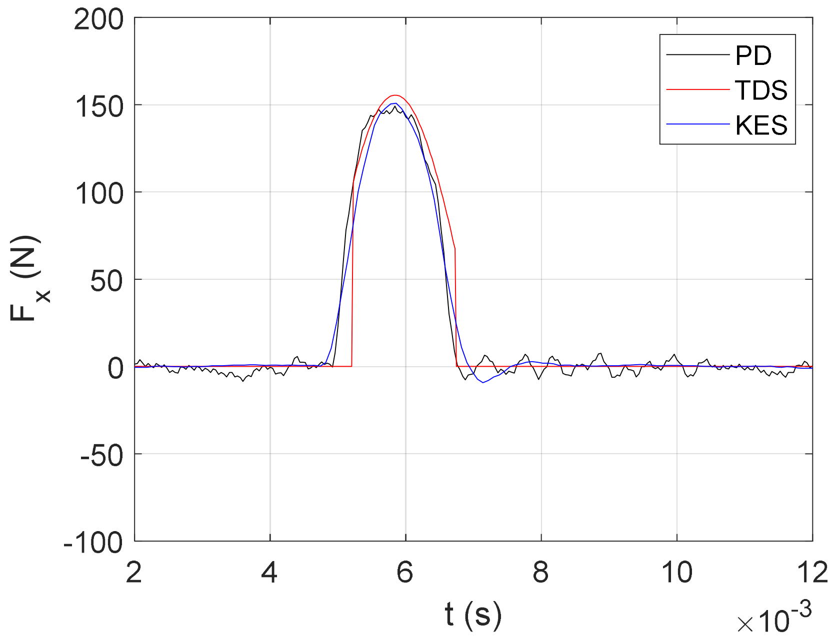

Figure 5.5. *X*-direction force comparison of the PD, TDS, and KES for a single tooth passing at a feed per tooth of 0.125 mm/tooth.

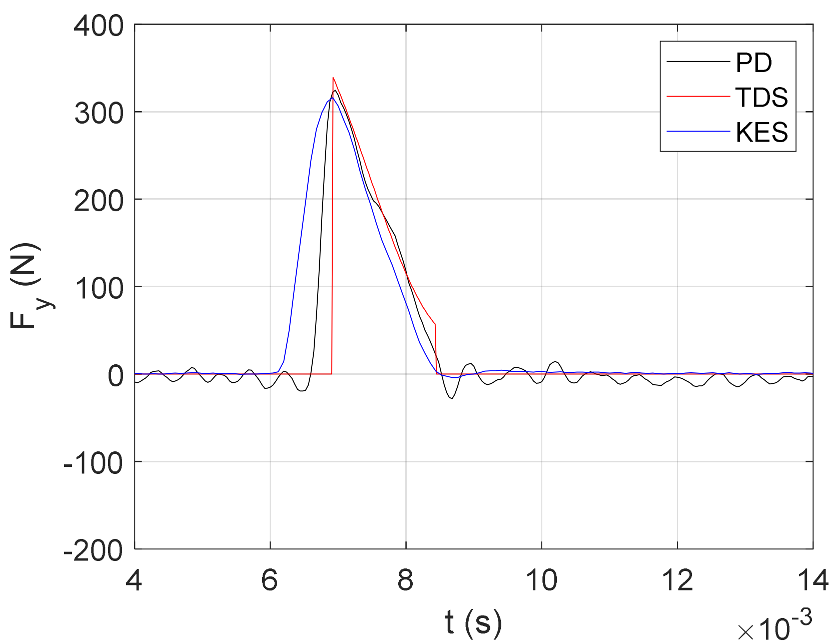

Figure 5.6. *Y*-direction force comparison of the PD, TDS, and KES for a single tooth passing at a feed per tooth of 0.125 mm/tooth.

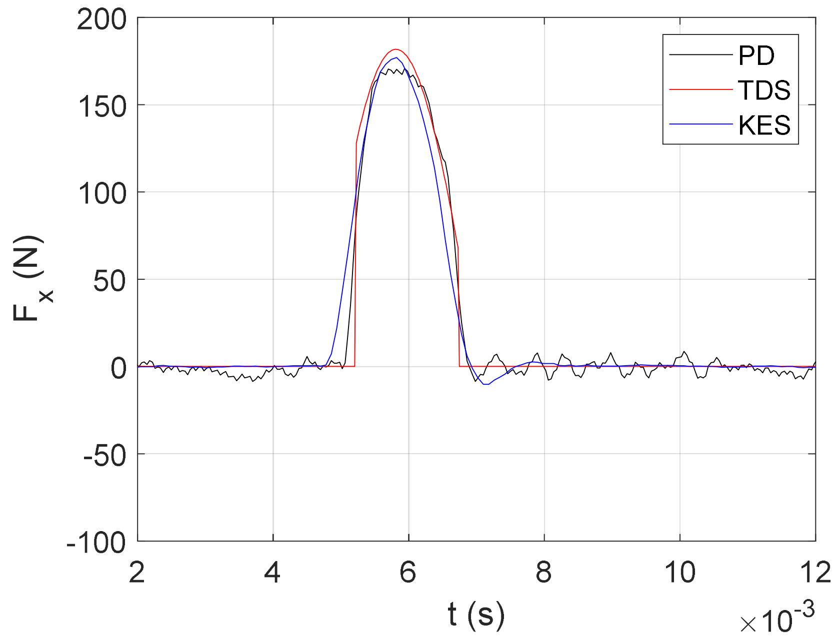

Figure 5.7. *X*-direction force comparison of the PD, TDS, and KES for a single tooth passing at a feed per tooth of 0.150 mm/tooth.

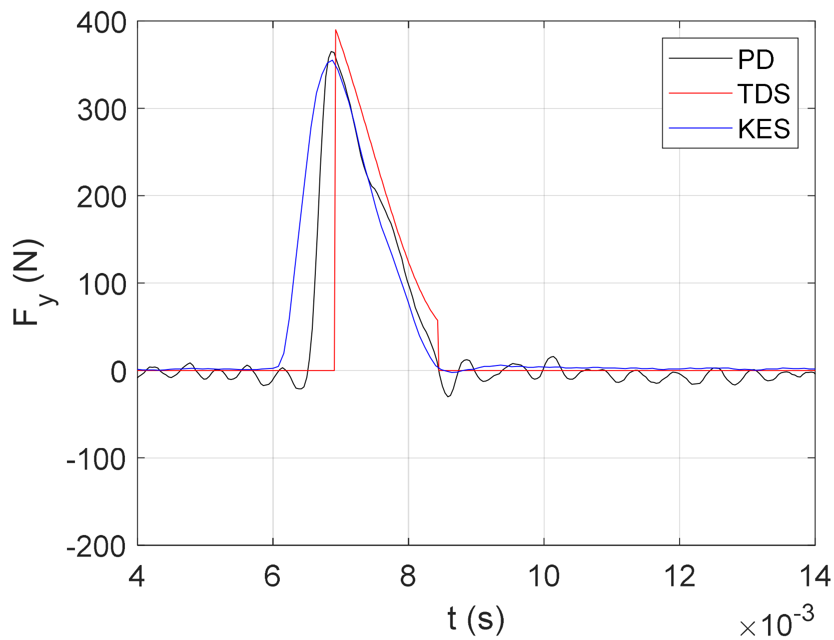

Figure 5.8. *Y*-direction force comparison of the PD, TDS, and KES for a single tooth passing at a feed per tooth of 0.150 mm/tooth.

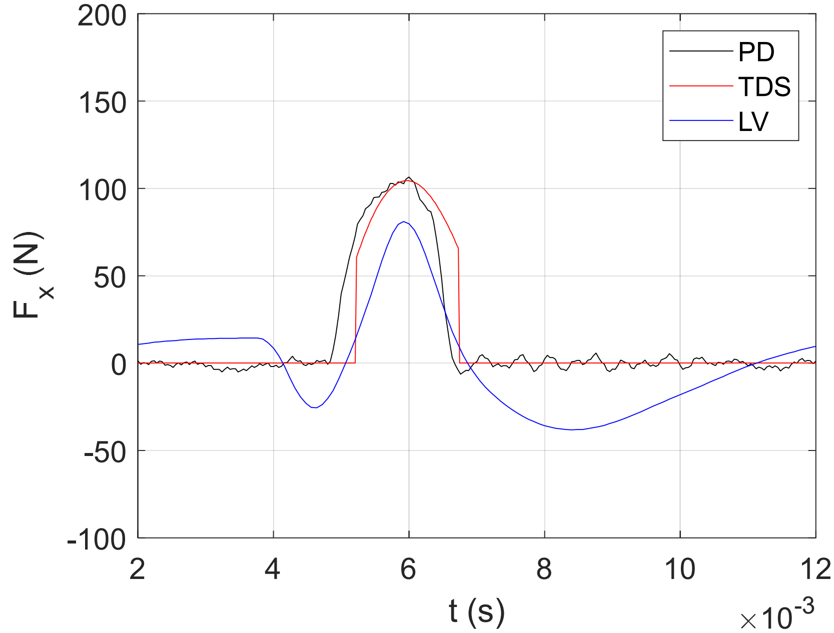

Figure 5.9. *X*-direction force comparison of the PD, TDS, and LV for a single tooth passing at a feed per tooth of 0.075 mm/tooth.

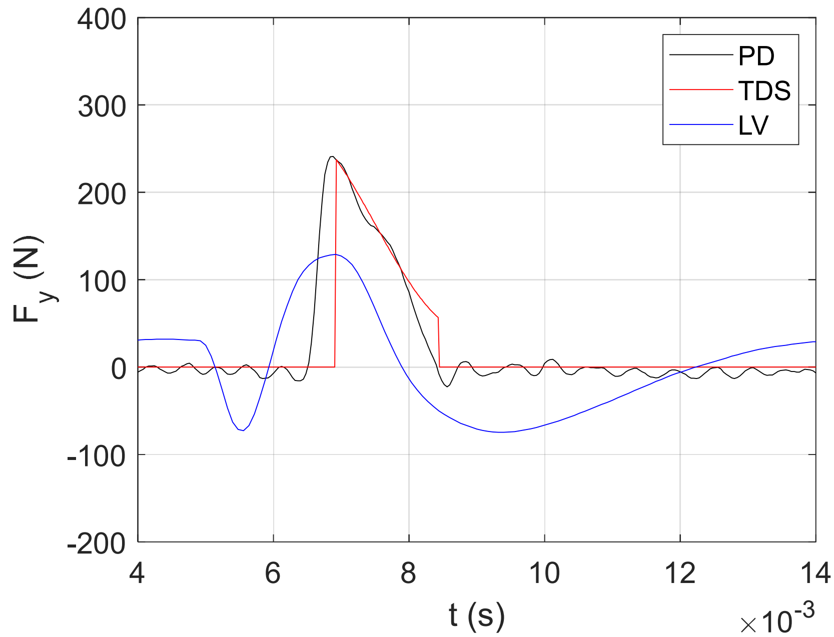

Figure 5.10. *Y*-direction force comparison of the PD, TDS, and LV for a single tooth passing at a feed per tooth of 0.075 mm/tooth.

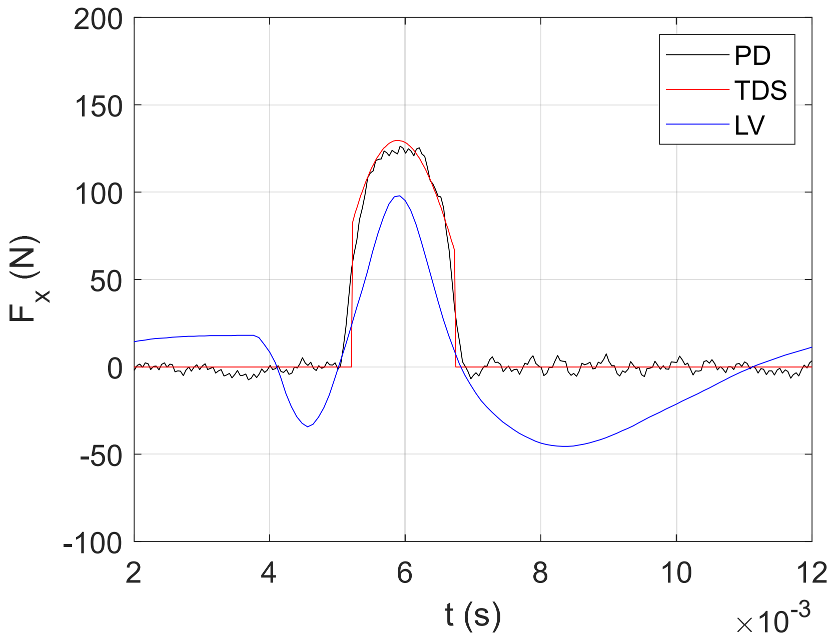

Figure 5.11. *X*-direction force comparison of the PD, TDS, and LV for a single tooth passing at a feed per tooth of 0.100 mm/tooth.

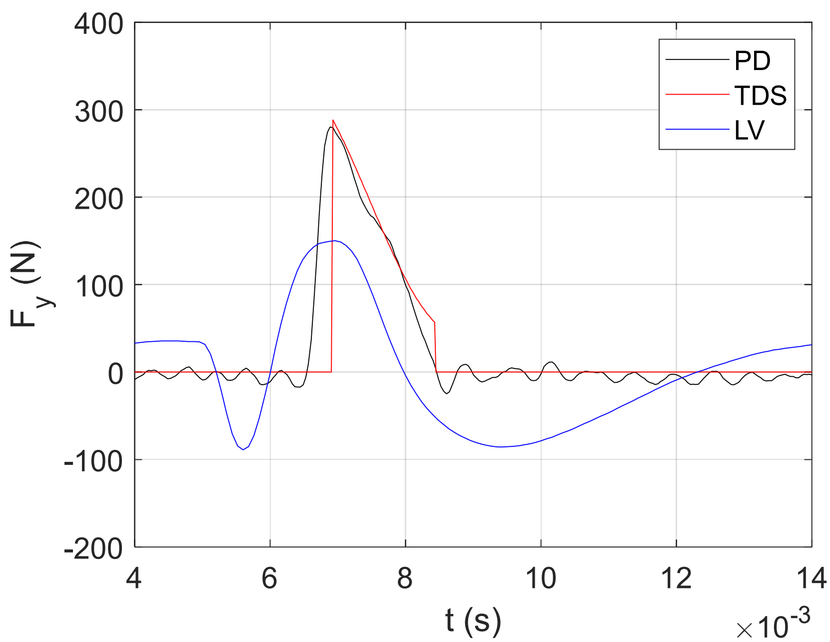

Figure 5.12. *Y*-direction force comparison of the PD, TDS, and LV for a single tooth passing at a feed per tooth of 0.100 mm/tooth.

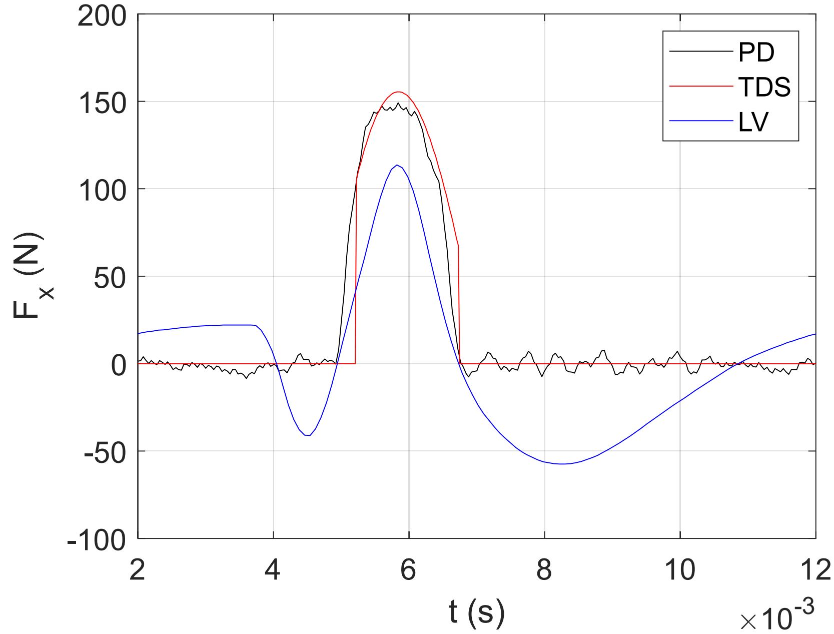

Figure 5.13. *X*-direction force comparison of the PD, TDS, and LV for a single tooth passing at a feed per tooth of 0.125 mm/tooth.

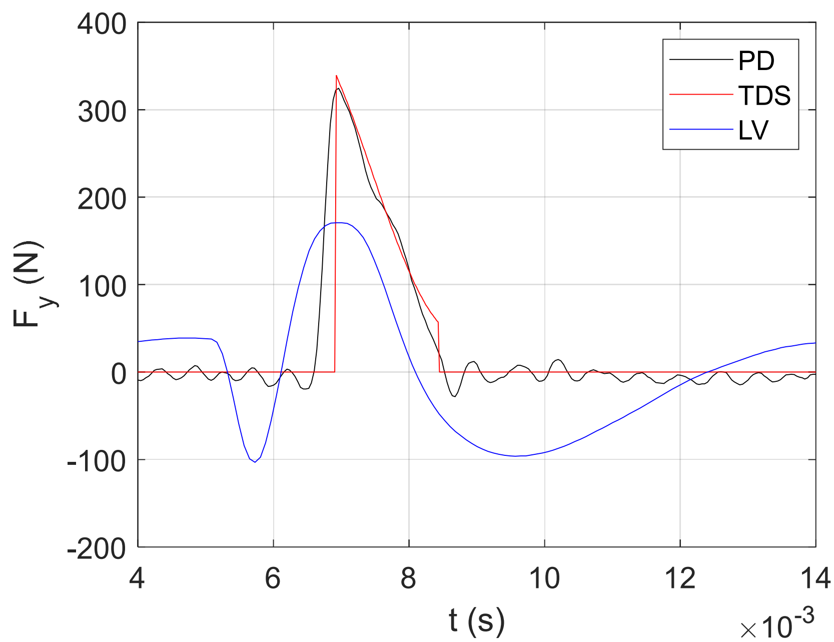

Figure 5.14. *Y*-direction force comparison of the PD, TDS, and LV for a single tooth passing at a feed per tooth of 0.125 mm/tooth.

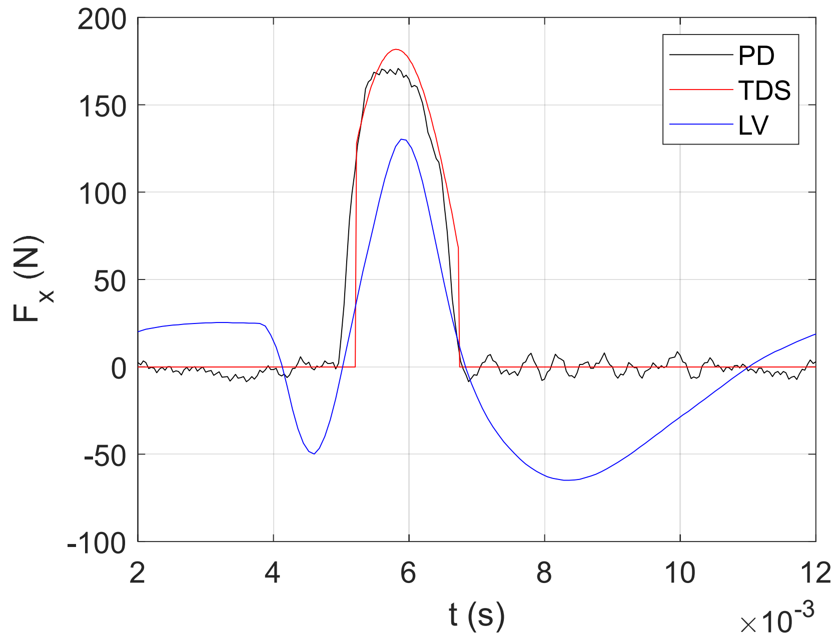

Figure 5.15. *X*-direction force comparison of the PD, TDS, and LV for a single tooth passing at a feed per tooth of 0.150 mm/tooth.

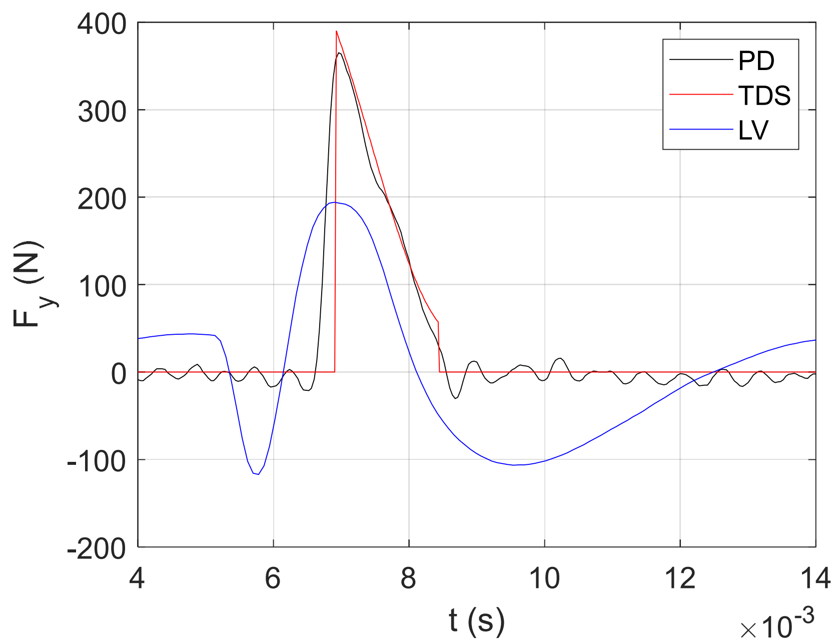

Figure 5.16. *Y*-direction force comparison of the PD, TDS, and LV for a single tooth passing at a feed per tooth of 0.150 mm/tooth.

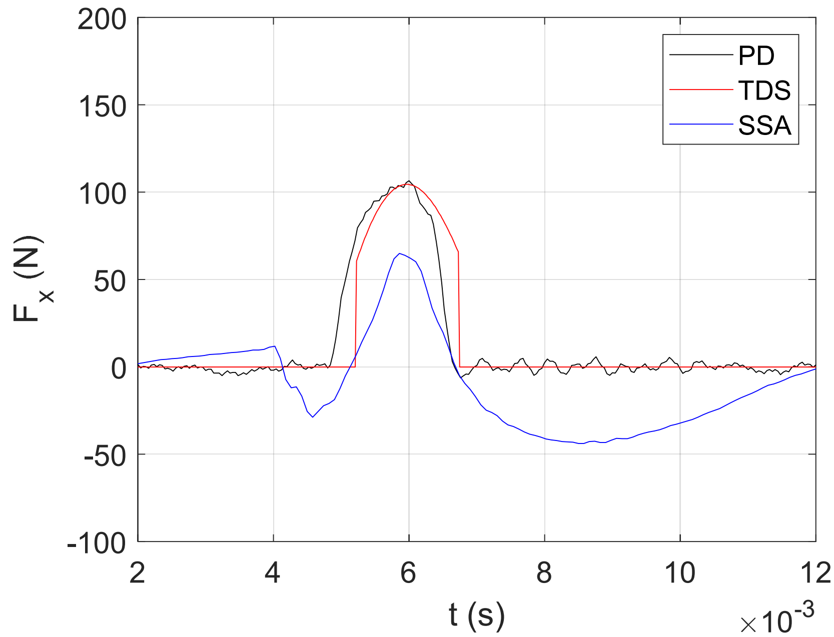

Figure 5.17. *X*-direction force comparison of the PD, TDS, and SSA for a single tooth passing at a feed per tooth of 0.075 mm/tooth.

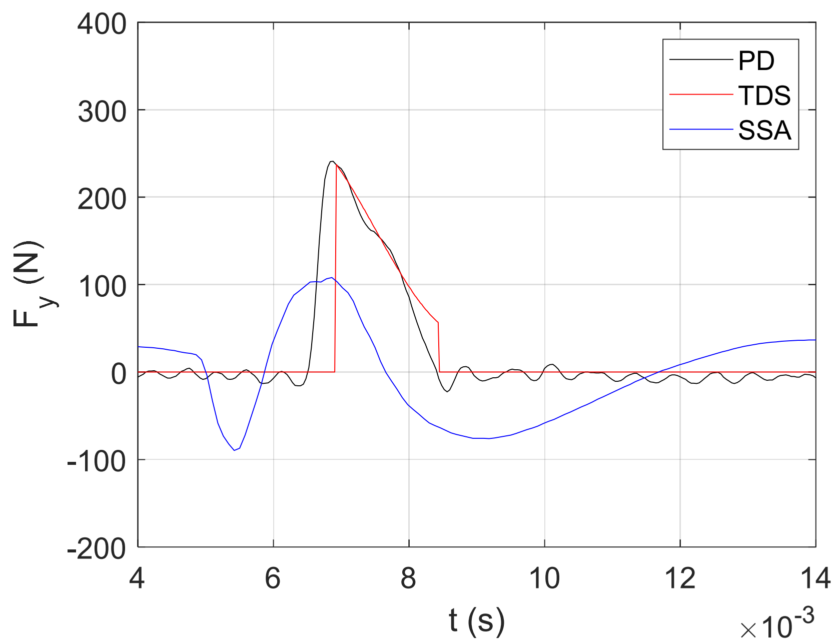

Figure 5.18. *Y*-direction force comparison of the PD, TDS, and SSA for a single tooth passing at a feed per tooth of 0.075 mm/tooth.

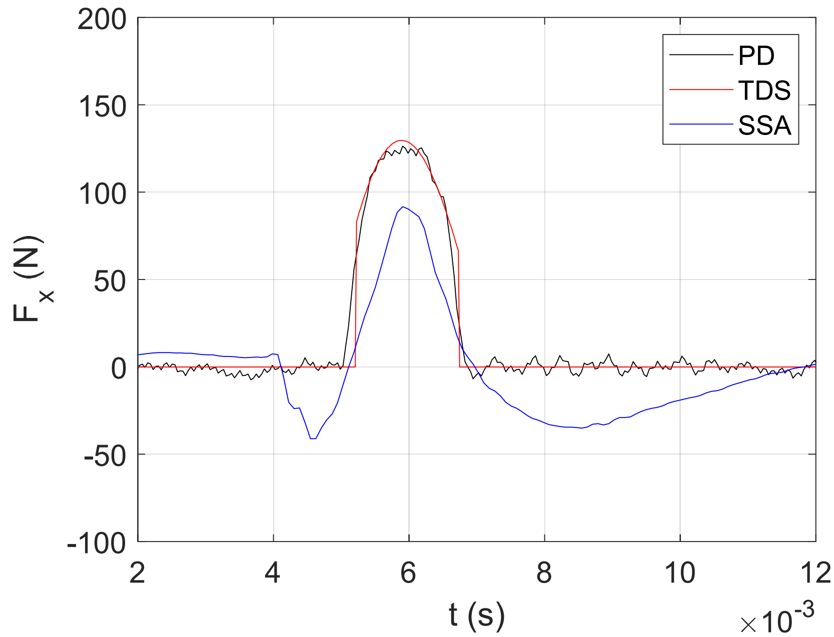

Figure 5.19. *X*-direction force comparison of the PD, TDS, and SSA for a single tooth passing at a feed per tooth of 0.100 mm/tooth.

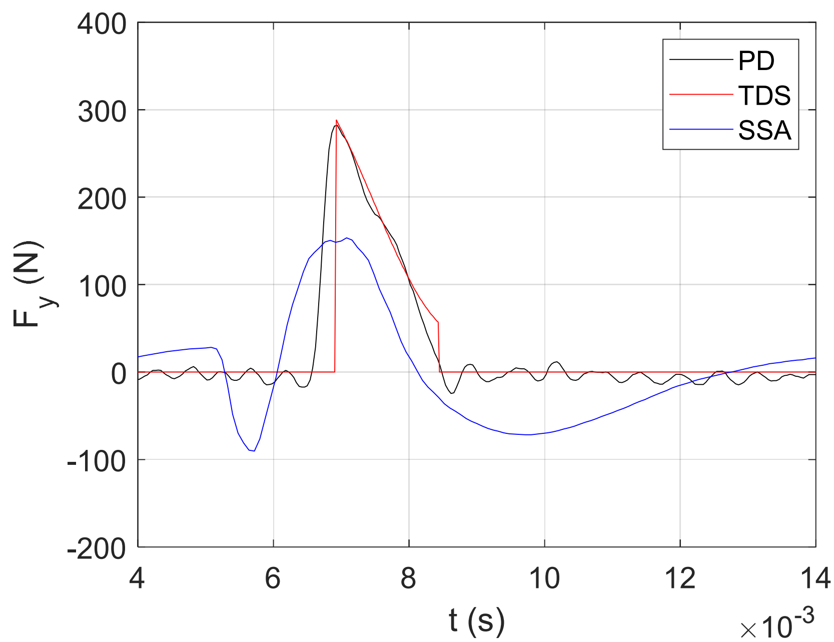

Figure 5.20. *Y*-direction force comparison of the PD, TDS, and SSA for a single tooth passing at a feed per tooth of 0.100 mm/tooth.

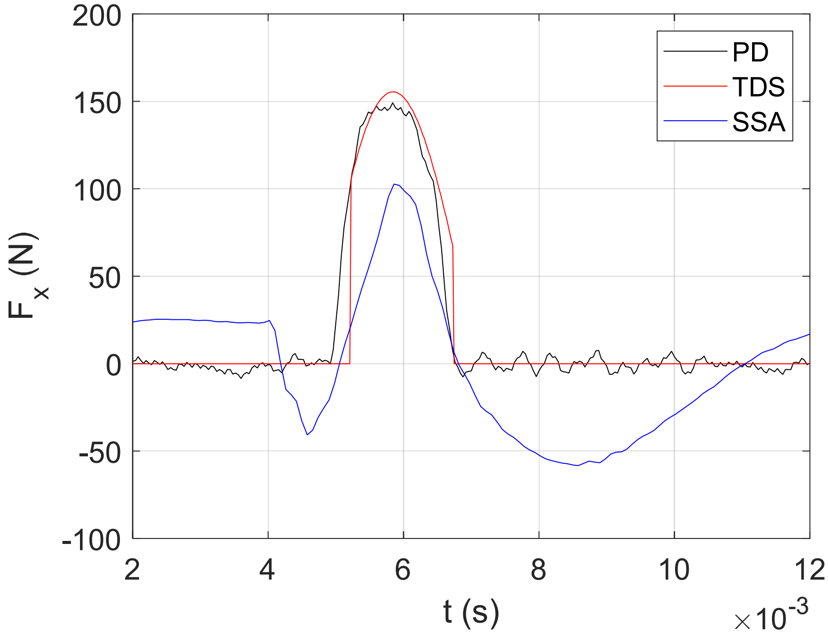

Figure 5.21. *X*-direction force comparison of the PD, TDS, and SSA for a single tooth passing at a feed per tooth of 0.125 mm/tooth.

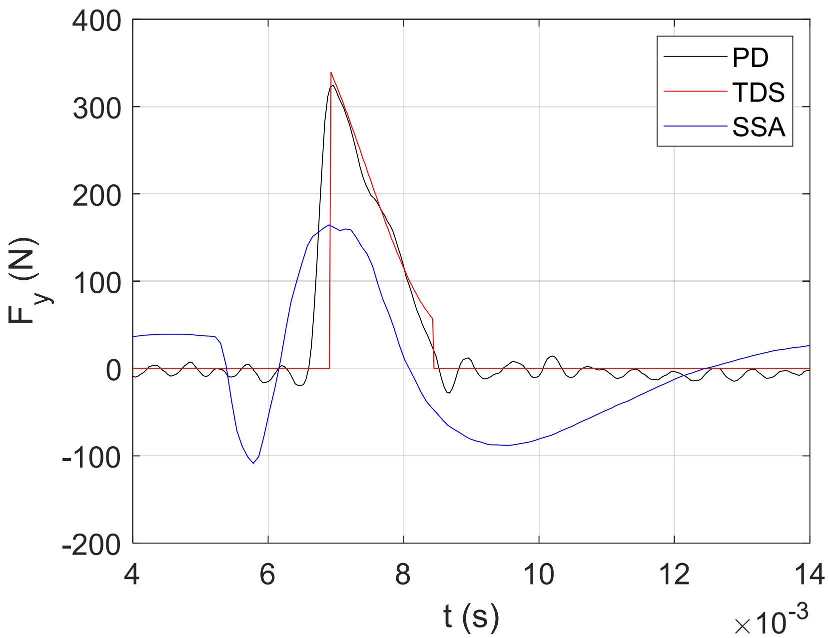

Figure 5.22. *Y*-direction force comparison of the PD, TDS, and SSA for a single tooth passing at a feed per tooth of 0.125 mm/tooth.

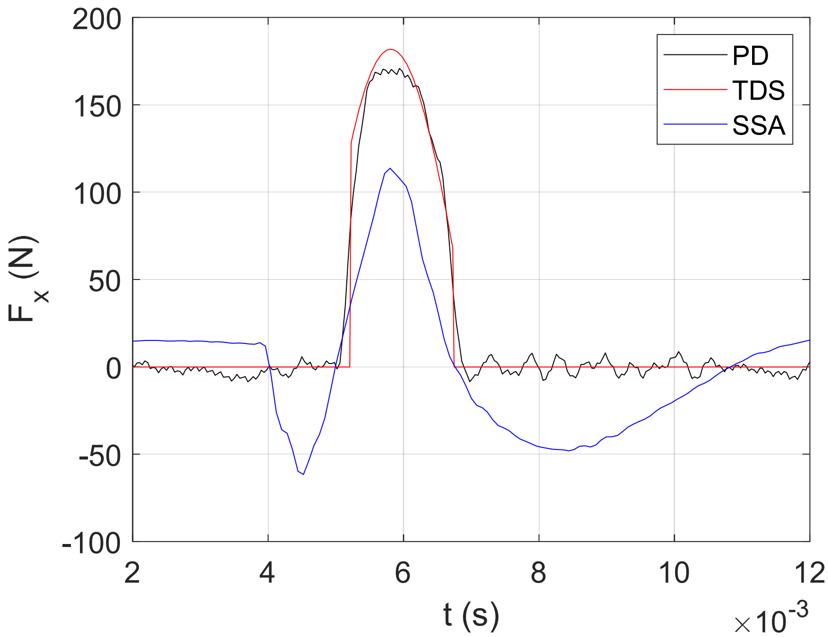

Figure 5.23. *X*-direction force comparison of the PD, TDS, and SSA for a single tooth passing at a feed per tooth of 0.150 mm/tooth.

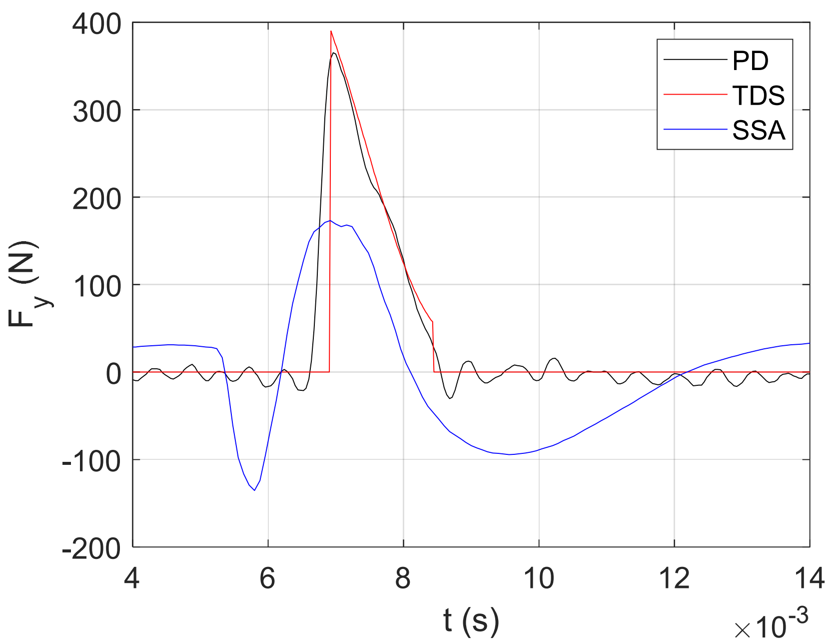

Figure 5.24. *Y*-direction force comparison of the PD, TDS, and SSA for a single tooth passing at a feed per tooth of 0.150 mm/tooth.

Piezoelectric Accelerometer (PA)

In this section, the experimental cutting forces measured by the PA are compared to those of the forces measured by the PD as well as to the forces produced by the TDS. The experimental cutting forces were obtained using the cutting parameters Table 5.1.

The *x*-direction and *y*-direction forces for a single tooth passing at the four feed per tooth values are shown in Figure 5.25 to Figure 5.32. For all of the feeds in both directions, the maximum forces measured by the PA are consistently less than the maximum forces of the PD and TDS. This is due to the mean value of the acceleration signal being zero; the mean value of the force was lost in the PA data analysis. To compensate for this, the difference between the maximum and minimum values for a single tooth passage was calculated from the PA data and used to compare to the peak values for the PD and TDS.

Comparison

In this section, the forces determined by all sensors are compared against the TDS. As mentioned previously, the LV, SSA, and PA sensors recorded only dynamic values; the mean value was zero. Therefore, the forces obtained from analyzing the LV, SSA, and PA signals did not retain the mean value. To enable comparison between the LV, SSA, and PA and KES, PD, and TDS, the peak-to-valley values for the forces determined by the LV, SSA, and PA were compared to the peak values from the KES, PD, and TDS.

Once the values for each sensor were obtained, the percent difference between the TDS and each sensor was calculated for both the *x*-direction and the *y*-direction forces. The results are provided in Figure 5.33 and Figure 5.34, respectively. In general, the KES and PD provide the best agreement with TDS. The LV generally provides the worst agreement. Because the LV, SSA, and PA sensors each lose the mean value of the cutting force during the frequency domain analysis, their value for dynamic force measurement is limited.

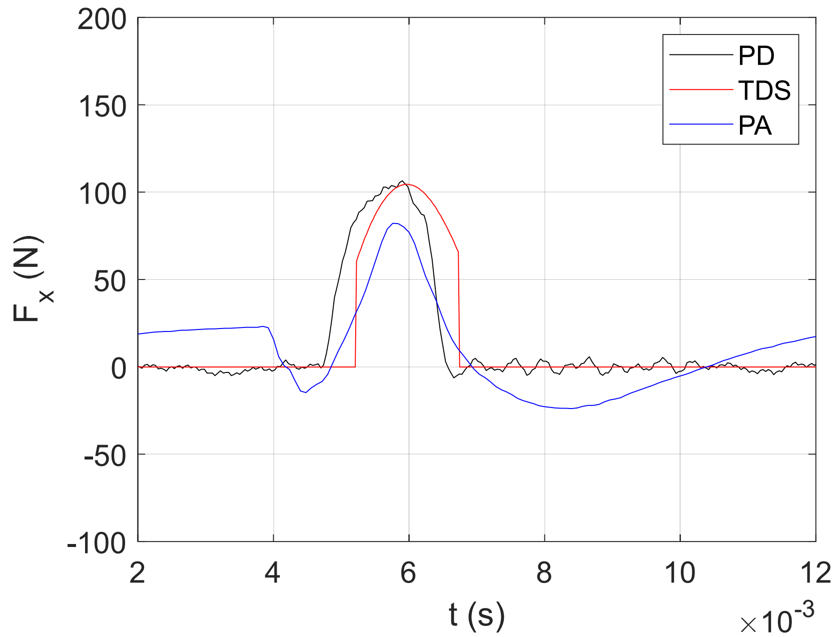

Figure 5.25. *X*-direction force comparison of the PD, TDS, and PA for a single tooth passing at a feed per tooth of 0.075 mm/tooth.

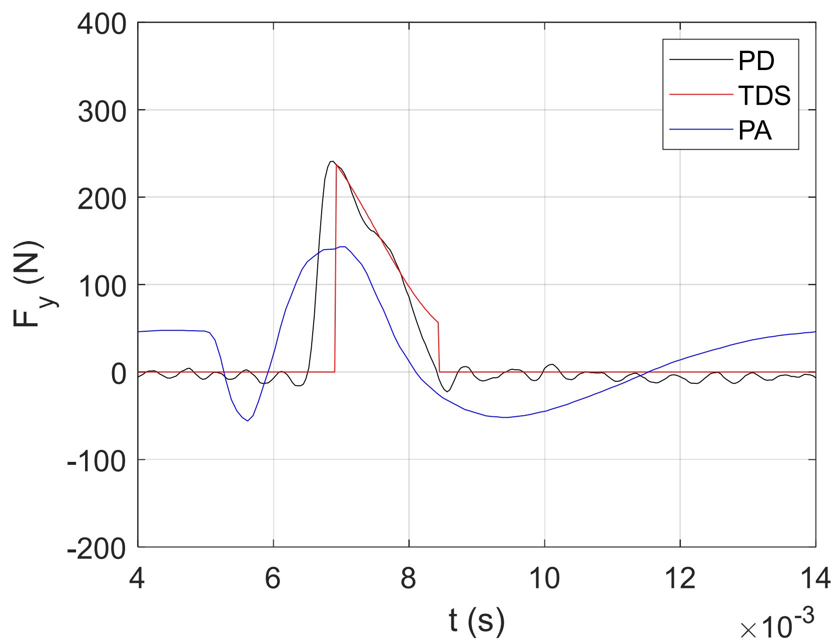

Figure 5.26. *Y*-direction force comparison of the PD, TDS, and PA for a single tooth passing at a feed per tooth of 0.075 mm/tooth.

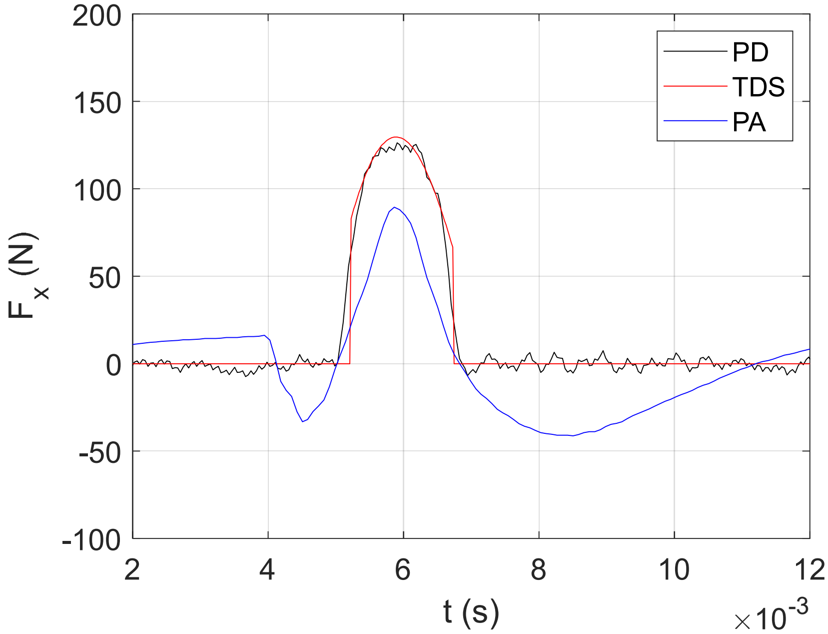

Figure 5.27. *X*-direction force comparison of the PD, TDS, and PA for a single tooth passing at a feed per tooth of 0.100 mm/tooth.

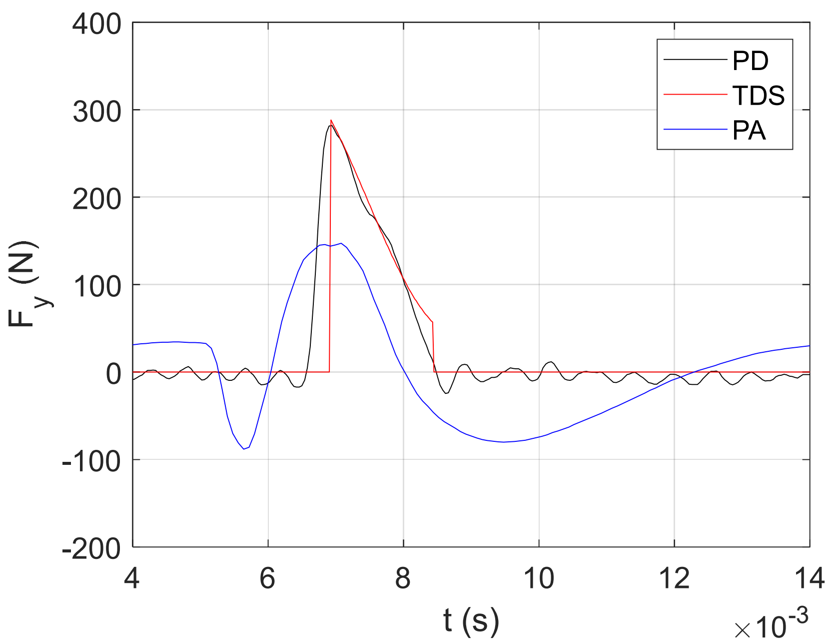

Figure 5.28. *Y*-direction force comparison of the PD, TDS, and PA for a single tooth passing at a feed per tooth of 0.100 mm/tooth.

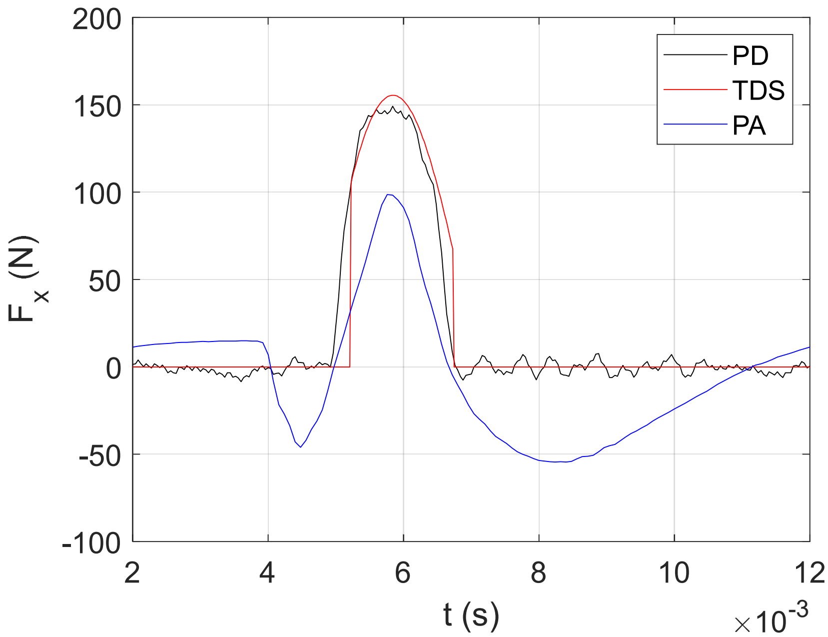

Figure 5.29. *X*-direction force comparison of the PD, TDS, and PA for a single tooth passing at a feed per tooth of 0.125 mm/tooth.

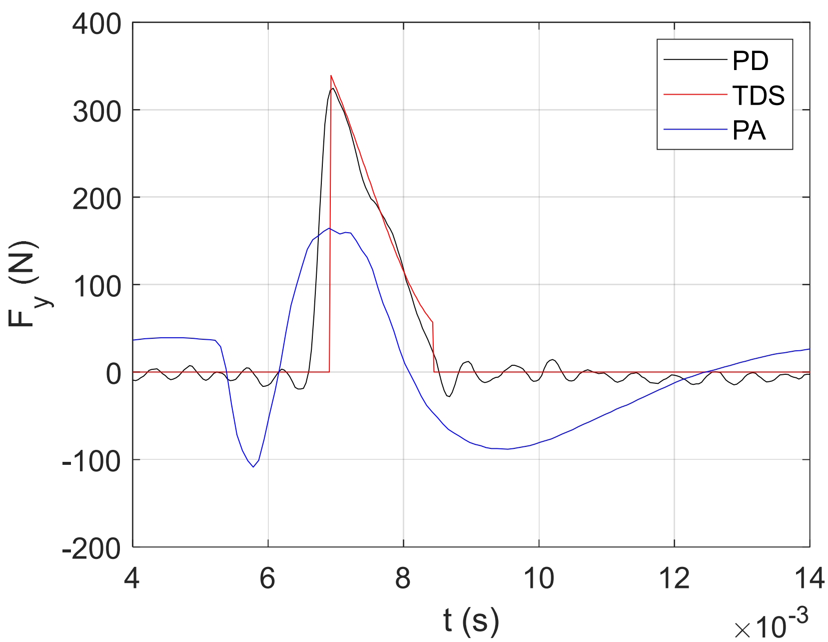

Figure 5.30. *Y*-direction force comparison of the PD, TDS, and PA for a single tooth passing at a feed per tooth of 0.125 mm/tooth.

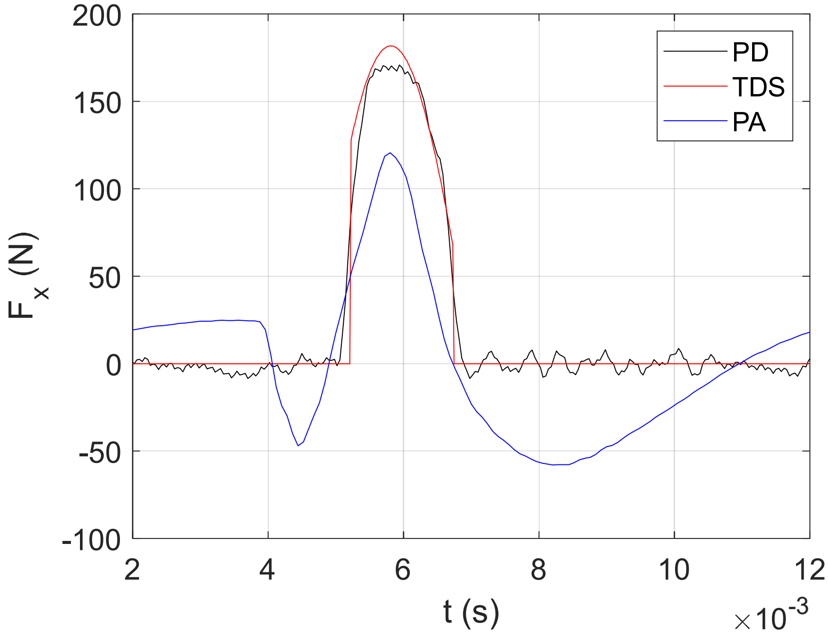

Figure 5.31. *X*-direction force comparison of the PD, TDS, and PA for a single tooth passing at a feed per tooth of 0.150 mm/tooth.

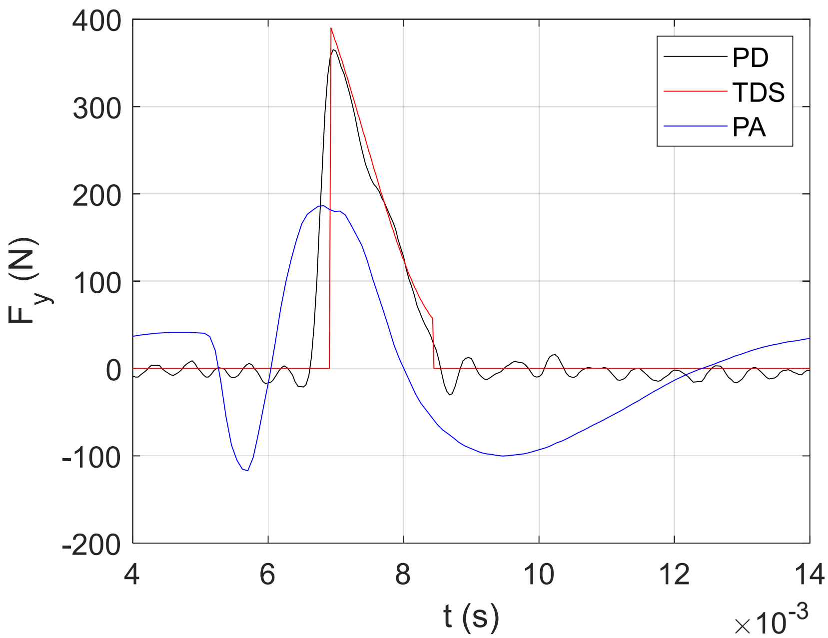

Figure 5.32. *Y*-direction force comparison of the PD, TDS, and PA for a single tooth passing at a feed per tooth of 0.150 mm/tooth.

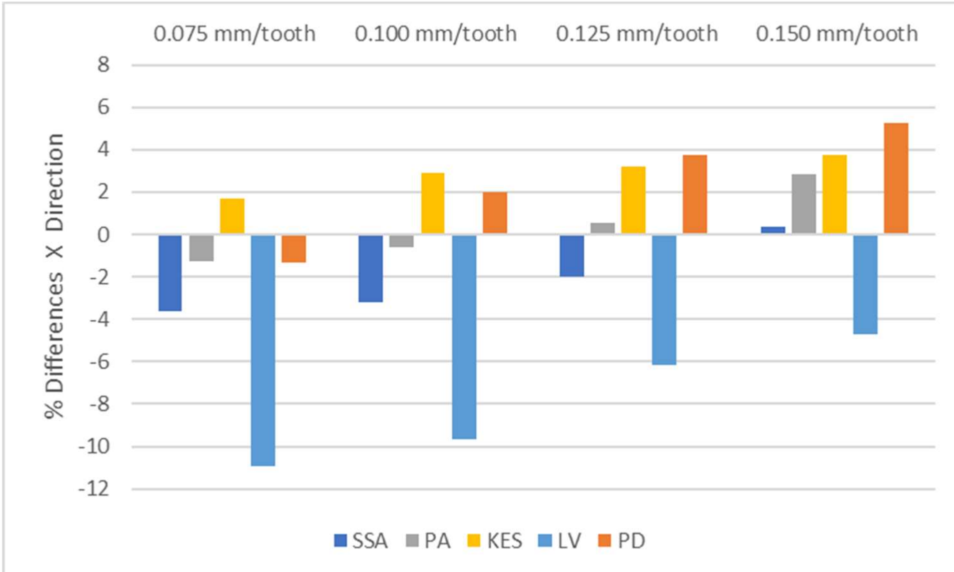

Figure 5.33. Percent difference between the *x*direction force determined by the TDS and the *x*-direction force as determined by the SSA, PA, KES, LV, and PD.

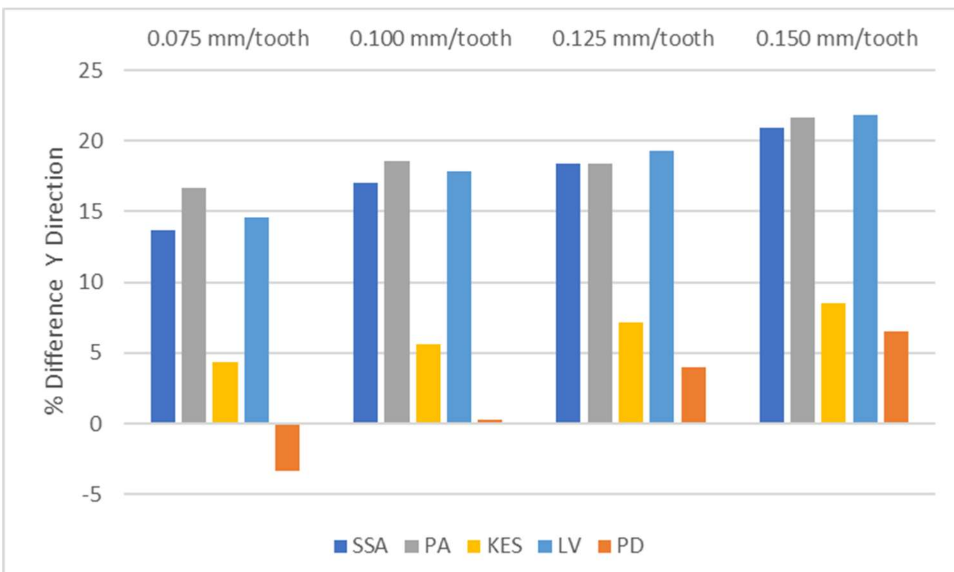

Figure 5.34. Percent difference between the *y*-direction force determined by the TDS and the *y*-direction force as determined by the SSA, PA, KES, LV, and PD.

CHAPTER 6: CONCLUSIONS

Cutting force for a milling operation were determined using a constrained motion dynamometer (CMD) and inverse force filtering. To accomplish this, the displacement, velocity, and acceleration of a workpiece mounted to the CMD moving stage were measured during milling using various sensors. The outputs of each sensor were converted to the frequency domain and convolved with their respective inverse frequency response functions to produce a frequency domain force. The force was converted back to the time domain for comparison with the forces measured by a piezoelectric dynamometer and the force predicted by a time domain simulation. This research distinguished itself from previous work by using velocity and acceleration measurements obtained from a CMD to determine cutting force.

The CMD comprised a single degree of freedom moving base attached to a frame by four flexure leaves. A knife edge sensor was used to measure the displacement of the workpiece mounted to the CMD moving state during milling. A laser vibrometer was used to measure the velocity of the workpiece. Both a solid state accelerometer and a piezoelectric accelerometer were used to measure the acceleration of the workpiece.

Each measurement signal was transferred to the frequency domain using the fast Fourier transform (FFT). The frequency domain displacement was then convolved with the inverse receptance frequency response function (FRF), the dynamic stiffness, to give force. The frequency domain velocity was convolved with the inverse mobility FRF, or mechanical impedance. It was also convolved with a band pass filter to attenuate unwanted signal amplification resulting from the mechanical impedance. The frequency domain acceleration was convolved with the inverse accelerance FRF, or dynamic mass, to yield force. It was also convolved with a lowpass filter to attenuate low frequency amplification due to the dynamic mass and a highpass filter to attenuate high frequency noise associated with the accelerometers. The resulting forces were converted back to the time domain by the inverse FFT.

The forces determined from the velocity and acceleration signals lost their average (or mean, or zero-frequency/DC) content and, therefore, only their peak-to-valley values could be used for comparison. Given the loss of DC content, and the extra filtering required, no advantages were observed when using the velocity and acceleration measurements to determine force. The knife edge sensor retained its DC content and therefore provided the only viable milling force signal. Although it was possible to determine the peak-to-valley force values from the velocity and acceleration signals, no real advantage was gained. The accelerometers were both comprised of a single component, making them easier to attach to the CMD than the knife edge sensor, which required an optical interrupter and a knife edge. When compared to one another, the accelerometers provided similar results, despite their different operating principles and price points. The laser vibrometer offered contactless force measurements, but the results did not warrant the high cost of the system.

LIST OF REFERENCES

[1] Gomez, M. and Schmitz, T., 2022, Stability Evaluation for a Damped, Constrained-motion Cutting Force Dynamometer, Journal of Manufacturing and Materials Processing, 6: 23.

[2] Gomez, M., Honeycutt, A., and Schmitz, T., 2021, Hybrid Manufactured Dynamometer for Cutting Force Measurement, Manufacturing Letters, 29: 65-69.

[3] Gomez, M. and Schmitz, T., 2020, Low-cost, Constrained-motion Dynamometer for Milling Force Measurement, Manufacturing Letters, 25: 34-39.

[4] Gomez, M. and Schmitz, T., 2019, Displacement-based Dynamometer for Milling Force Measurement, Procedia Manufacturing, 34:867-875.

[5] Zameroski, R., Gomez, M., and Schmitz, T., 2022, Geometry-based, Gaussian Profile Model for Optical Knife-edge Displacement Sensor, Precision Engineering, 73: 470-476.

[6] Schmitz, T.L., Smith, K.S., 2009, Machining Dynamics: Frequency Response to Improved Productivity, Springer, New York, NY.

[7] Altintas, Y., 2012, Manufacturing Automation: Metal Cutting Mechanics, Machine Tool Vibrations, and CNC Design, Cambridge University Press.

[8] Tlusty, J., 2000, Manufacturing Processes and Equipment, Prentice Hall, Upper Saddle River, NJ.

[9] Tlusty, J., Andrews, G. C., 1983, A Critical Review of Sensors for Unmanned Machining, CIRP Annals, 32: 563-572.

[10] Byrne, G., Dornfeld, D., Denkena, B., 2004, Advanced cutting technology, CIRP Annals, 52:483-507.

[11] Tlusty, J., Jang, D., Tarng, Y., 1987, Measurements of the milling force over a wide frequency range, Proceedings of the 15th NAMRC, 273-280.

[12] Teti, R., Jemielniak, K., O'Donnel, G., Dornfeld, D., 2010, Advanced monitoring of machining operations, CIRP Annals, 59:707-739.

[13] Gautschi, G.H., 2002, Piezoelectirc Sensorics, Springer Berlin Heidelberg, Berlin, Germany

[14] Gautschi, G.H., 1972, Cutting forces in machining and their routine measurement with multi-component piezo-electric force transducers, Proc. 12th Int. Mach. Tool design and research, 113-120.

[15] Kistler Instrumente AG, 2007, The Piezoelectric Effect, Theory, Design and Usage, Company White Paper.

[16] Altintas, Y., Yellowley, I., 1989, The process detection of tool failure in milling using cutting force models, ASME J. of Eng. For Industry, 111: 149- 157.

[17] Altintas, Y., Yellowley, I., Tlusty, J., 1985, Detection of tool breakage in milling, Transactions of the ASME, 18:41-48.

[18] Altintas, Y., 1988, In process detection of tool breakage using time series monitoring of cutting forces, Int. J. Mach. Tools and Manuf., 28: 157-172.

[19] Burton, D., Duncan, G.S., Ziegert, J.C., Schmitz, T.L., 2004, High frequency, low force dynamometer for micro-milling force measurement, Proceedings of the 19th American Society for Precision Engineering Annual Meeting, 221-224.

[20] Korkut, I., 2003, A dynamometer design and its construction for milling operation, Materials and Design, 24: 631-637.

[21] Yalidz, S., Unsacar, F., 2006, A dynamometer design for measurement of cutting forces on turning, Measurement, 39: 80-89.

[22] Yaldiz, S., Unsacar, F., Haci, S., Isik, H., 2007, Design, development and testing of a four-component milling dynamometer for the measurement of cutting force and torque, Mechanical Systems and Signal Processing, 21, 1499-1511.
[23] Transchel, R. Stirnimann, J., Blattner, M., Bill, B., Thiel,R., Kuster, F., Wegener, K, 2012, Effective dynamometer for measuring high dynamic process force signals in micro machining operations, Procedia CIRP, 1, 558-562.
[24] Totis, G., Sortino, M., 2011, Development of a modular dynamometer for triaxial cutting force measurement in milling, Int. J. Mach. Tools Manuf., 51: 34-42.
[25] Totis, G., Adams, O., Sortino, M., Veselovac, D. Klocke, F., 2014, Development of an innovative plate dynamometer for advanced milling and drilling applications, Measurement, 49, 164-181.
[26] Totis, G., Wirtz, G., Sortino, M., Veselovac, Kuljanic, F., D. Klocke, F., 2010, Development of a dynamometer for measuring individual cutting edge forces in face milling, Mechanical Systems and Signal Processing,24/6: 1844-1857.
[27] Jun, M., Ozdoganlar, B., DeVor, R., Kapoor, S., Kirchheim, K., Schnaffer, G., 2002, Evolution of spindle-based force sensor for monitoring and fault diagnosis of machining operations, Int. J. of Mach. Tools and Manuf., 42: 741-751.
[28] O'Donnel, G.E., Kelly, K., Byrne, G., 2000, Use of a sensor integrated motor spindle for monitoring of a flexible machining center, 2nd CIRP Int. Sem. On ICME, 383-388.
[29] Byrne, G., O'Donnell, G.E., 2007, An integrated force sensor solution for process monitoring of drilling operations, CIRP Annals, 56: 59-62.
[30] Smith, D.A., Smith, S., Tlusty, J., 1988, High performance milling torque sensor, J. of Manuf. Sci. and Eng., 120: 504-514.
[31] Park, S.S., Altintas, Y., 2004, Dynamic compensation of spindle-integrated force sensors, CIRP Annals, 53/1: 305-308.
[32] Park, S.S., 2003 High frequency bandwidth cutting force measurements in milling using the spindle integrated force sensor system, Dept. of Mech. Eng., Univ. of British Columbia, PhD. Thesis.
[33] Aoyama, H., Ishii, T., 2004, Sensor to detect cutting force components, cutting torque, and cutting tool deflections, J. of Manufacture Processing, 6: 141-147.
[34] Ettrichrätz, M., Drossel, W., Gebhardt, S., Bucht, A., Kranz, B., Schneider, J., 2018, Performance of a new piezoceramic thick film sensor for measurement and control of cutting forces during milling, CIRP Annals, 67/1, 45-48.
[35] Tounsi, N., Otho, A., Dynamic cutting force measuring, 2000, Int J. Mach. Tools Manuf., 40: 1157-1170.
[36] Tounsi, N., Otho, A., Dynamometer performance modeling and experimental assessment, 2000, J. Dyn. Syst. Meas. Control, Transactions of the ASME, 122: 477-482.
[37] Park S.S., Chae, J., 2007, High frequency bandwidth measurements of micro cutting forces, Int. J. Mach. Tools Manuf., 47:1433–1441.
[38] Albrecht, A., Park, S.S., Altintas, Y., Pritschow, G., 2005, High frequency bandwidth cutting force measurement in milling using capacitance displacement sensors. Int. J. Mach. Tools Manuf.; 45:993–1008.
[39] Totis, G., Dombovari, Z. Sortino, M., 2020, Upgraded Kalman filtering of cutting forces in milling, Sensors 20, 5398: 1-21.

[40] Castro, L.R., Vieville, P., Lipinski, P., 2006, Correction of dynamic effects on force measurements made with piezoelectric dynamometers, Int. J. of Mach. Tools Manuf., 46: 1707-1715.

[41] Korkmaz, E., Bediz, B., Gozen, B.A., Ozdoganlar, O.B., 2014, Dynamic characterization of multi-axis dynamometers, Prec. Engineering, 38: 148- 161.

[42] Ozdoganlar, O.B., Korkmaz, E., Gozen, B.A., Bediz, B., 2015, Highfrequency compensation of dynamic distortions in micromachining force measurements, Procedia Manufacturing, 1: 534-545.

[43] Bediz, B., Korkomaz, E., Ozdoganlar, O.B., 2014, An impact excitation system for repeatable, high-bandwidth modal testing of miniature structures, J. of Sound and Vibration, 333: 2743-2761.

[44] Ozdoganlar, O.B., Hansche, B.D., Carne, T.G., 2005, Experimental modal analysis for microelectromechanical systems, Exp. Mechanics, 46: 498- 506.

[45] Scippa, A., Sallese, L., Grossi, N., Campatelli, G., 2015, Improved dynamic compensation for accurate cutting force measurements in milling applications, Mech. Syst. and Sig. Processing, 54-55, 314-324.

[46] Chung, Y.L., Spiewak, S.A., 1994, A model of high-performance dynamometer., J. of Eng. for Industry, 116:279-288.

[47] Spiewak, S.A., Di Corpo, J., 1991, Adaptive compensation of dynamic characteristics for in-process sensors. J. of Eng. for Industry, 113: 198-206.

[48] Mangnevall, M., Lundblad, M., Ahlin, K., Broman, G., 2012, High frequency measurements of cutting forces in milling by inverse filtering, Mach. Sci. and Technology, 16: 487-500.

[49] Wan, M., Yin, W., Zhang, W., Liu, H., 2017, Improved inverse filter for the correction of distorted measured cutting forces, Int. J. Mechanical Sciences, 120, 276-285.

[50] Smith, S., & Tlusty, J. 1991, An overview of modeling and simulation of the milling process, J. of Eng. For Industry, 113: 169-175.

[51] Gomez, M, 2020, Displacement based force dynamometer for milling force measurement, Doctoral Dissertation, University of Tennessee. https://trace.tennessee.edu/utk_graddiss/6654/

[52] Analog Devices, ADXL 1003z: Low noise, wide bandwidth, MEMS accelerometer [Data Sheet]. https://www.analog.com/media/en/technical-documentation/data-sheets/ADXL1003.pdf

[53] Elies, Stephan, 2015, Performance analysis of commercial accelerometers: A parameter review, Sensors & Transducers 193.10: 179.

VITA

Zachary Mason was born and raised in Knoxville, Tennessee. He obtained his bachelor's degree in aerospace engineering from the Georgia Institute of Technology in 2014. After working as an engineer for an aerospace contractor, he obtained his Juris Doctor from the University of Tennessee College of Law, graduating in 2020. In 2021, he began his M.S. in aerospace engineering, at the University of Tennessee. While studying, he began researching under Dr. Tony Schmitz at the Machine Tool Research Center, focusing on low-cost alternatives for machine force measurement.